Application of polystyrene sulfonate (PSS) for inhibiting toxicity of ALS/FTD-linked dipeptide repeats

Anna Bratek-Skicki[1,2,7,*#], Junaid Ahmed[1,2,*], Karl Jonckheere[3], Eveline Peeters[3], Kara Heeren[4,5], Alex Volkov[1,2], Jelle Hendrix[6], Piotr Batys[7], Ludo Van Den Bosch[4,5], Peter Tompa[1,2,8,#]

[1]VIB-VUB Center for Structural Biology, Flemish Institute for Biotechnology, Brussels, Belgium

[2]Structural Biology Brussels, Vrije Universiteit Brussel (VUB), Brussels, Belgium

[3]Research Group of Microbiology, Department of Bioengineering Sciences (DBIT), Vrije Universiteit Brussel (VUB), Brussel, Belgium

[4]Department of Neurosciences, Experimental Neurology and Leuven Brain Institute, KU Leuven - University of Leuven, Leuven, Belgium

[5]VIB Center for Brain & Disease Research, Laboratory of Neurobiology, Leuven, Belgium

[6]Dynamic Bioimaging Lab, Advanced Optical Microscopy Centre, Biomedical Research Institute, Hasselt University, Hasselt, Belgium

[7]Jerzy Haber Institute of Catalysis and Surface Chemistry, Polish Academy of Sciences, Niezapominajek 8, PL-30239 Krakow, Poland

[8]Institute of Enzymology, Research Centre for Natural Sciences, Budapest, Hungary

[*]these two authors contributed equally to this work

[#]to whom correspondence should be addressed at: Anna.Bratek-Skicki@vub.be, and peter.tompa@vub.be

Abstract

The expansion of GGGGCC (G4C2) repeats in the noncoding region of C9orf72 is the most common genetic cause of familial and sporadic amyotrophic lateral sclerosis (ALS) and frontotemporal dementia (FTD). The repeat region is translated into five different dipeptide repeats (DPRs), of which the arginine-rich DPRs (R-DPRs) poly-GR (GRn) and poly-PR (PRn) are highly neurotoxic and are probably primarily responsible for the disease. Here, we characterized the protective effect against R-DPR toxicity of polystyrene sulfonate (PSS), an FDA-approved drug applied in hyperkalemia, in biochemical, cellular, and animal models of ALS/FTD. We found that PSS, in a length-dependent manner, interacts very tightly with R-DPRs, and releases their bound RNA in R-DPR - RNA mixtures. PSS significantly influences the liquid-liquid phase separation (LLPS) of R-DPRs elicited by RNA and reduces their ensuing cell toxicity in Neuro2a cells. PSS is cell penetrable, and it is also effective in countering the toxicity of R-DPRs in zebrafish embryos. Except for the longest (n = 340) variant, PSS is toxic neither to cells nor to mice upon intracerebroventricular injection up to 1 mM concentration. Our results suggest that its polymeric nature endows PSS with an advantageous effect in C9-ALS/FTD and offers a possible remedy against this debilitating neurodegenerative disease.

Introduction

Amyotrophic lateral sclerosis (ALS) and frontotemporal dementia (FTD) are severe neurodegenerative diseases that show significant genetic, pathomechanistic and clinical overlap. Both diseases encompass a progressive loss of neurons that usually leads to respiratory failure and death within 3 to 5 years after diagnosis [1-3].

About 90% of ALS/FTD cases are sporadic (sALS/FTD) with no apparent genetic predisposition, while approximately 10% are inherited (familial, fALS/FTD). The most prominent genes affected in fALS/FTD are superoxide dismutase 1 (SOD1), TAR DNA-binding protein (TARDBP, TDP-43), fused in sarcoma (FUS) and C9orf72 [4]. Among these, hexanucleotide (G4C2) repeat expansion (HRE) in the 5′ noncoding region of the C9orf72 gene is the most common genetic cause (40%) of fALS/FTD, hereafter referred to as C9-ALS/FTD [5]; C9orf72 HRE is also implicated in about 10% of sporadic (sALS/FTD) cases.

HRE may comprise three pathological mechanisms. The loss of function of C9orf72 protein may disturb autophagy pathways and endosomal trafficking [6]. Another potential mechanism assumes a toxic gain-of-function due to the production of mRNA containing an aberrant, expanded repeat region [7-9]. Recent studies, however, emphasize a toxic gain-of-function caused by the aberrant, repeat-associated, non-AUG (RAN) translation of C9orf72 mRNA into five dipeptide repeats (DPRs) [10, 11] being the most prevalent disease mechanism. Of the five different DPRs, poly-PR and poly-GR (R-DPRs) have been reported to be highly toxic [8, 12, 13] due to disrupting

cellular processes such as nucleocytoplasmic transport, RNA processing and the formation of cytoplasmic and nuclear ribonucleoprotein particles (condensates), such as stress granules (SGs) and nucleoli [14-16]. As they carry a very high net charge, R-DPRs can engage in tight interactions with RNA, they can undergo liquid-liquid phase separation (LLPS) and induce this process in combination with RNA and numerous proteins involved in RNA- and stress-granule metabolism, such as nucleophosmin 1 (NPM1) [17] and Ras GTPase-activating protein-binding protein 1 (G3BP1) [18]. R-DPRs are cell penetrable [16], they might serve as biomarkers of fALS/FTD [19], and due to their excessive toxicity, they are primary drug targets, although owing to their highly non-natural, disordered structure, they are considered mostly undruggable. It is to be emphasized that the gain-of-function mechanisms are also supported by direct observation of G4C2-HRE RNA- and DPR- containing inclusions in patients with C9-ALS/FTD [20, 21], and the three distinct mechanisms, as they have been studied independent of each other, do not have to be mutually exclusive [22].

There are only a few drugs approved by the U.S. Food and Drug Administration (FDA) to treat ALS/FTD, such as Radicava, Rilutek, Tigluik and Nuedexta, all of which work by indirect mechanisms. The active compound of Radicava is edaravone, a drug used to treat stroke [23]. The compound is an antioxidant, and its use rests on the hypothesis that oxidative stress contributes to neurodegeneration [24]. Rilutek and Tigluik incorporate riluzole, a sodium-channel inhibitor and antiglutamatergic compound that delays the onset of ventilator-dependence or tracheostomy in some patients, extending life expectancy by a few months [25]. Nuedexta contains two compounds, quinidine and dextromethorphan that can treat pseudobulbar effect (PBA) of uncontrolled episodes of laughing or crying in some patients with ALS and other neurological diseases, but its exact mechanism is unknown [26]. Most recently, an antisense oligonucleotide (ASO) against SOD1 has been approved by FDA as Tofersen [27], and another against C9orf72 mRNA is in clinical trials [28-30].

Unfortunately, with the exception of Tofersen, the approved drugs only mitigate symptoms and do not target basic mechanism(s) of the disease. Based on the extreme toxicity and cell-penetrating nature [31-33] of R-DPRs in many different cell types and model organisms, we have decided to take a radically different approach to tackle ALS/FTD caused by C9orf72-expansion. Quite recently, an “ultrahigh” (picomolar) affinity interaction between two oppositely charged intrinsically disordered proteins (IDPs), histone H1 and prothymosin-α, was reported [34]. By analogy, we thought that intrinsically disordered positive R-DPRs could be targeted by a highly negatively charged polymeric substance, polystyrene sulfonate (PSS) [35, 36]. PSS is an FDA-approved drug for treating hyperkalemia (cf. Suppl. Table S1), and due to its high negative charge, we hypothesized that it would engage in very tight binding with R-DPRs, counteract their LLPS and alleviate cellular toxicity of R-DPRs in disease. Accordingly, here we demonstrate that PSS can bind both poly-PR and poly-GR with a Kd of single-digit nM, it interferes with R-DPR LLPS and releases R-DPR-bound

RNA and has a remarkable protective effect in cellular and animal models of C9orf72-related ALS/FTD, as also outlined in a PCT patent application [37].

Results

Polystyrene sulfonate binds C9orf72 R-DPRs very tightly

Polystyrene sulfonate (PSS) is a negatively charged polyelectrolyte bearing sulfonate groups (Scheme 1). Due to the very low pKa of the sulfonate group (- 2.1), PSS is fully charged in a wide range of pH and ionic strength conditions. PSS is commonly used in additives [38], membranes [39], ion exchange resins [40], and personal care products [41]. PSS is also used as an FDA-approved drug to treat hyperkalemia in patients with renal insufficiency ([42], cf. Suppl. Table S1) and as an adjuvant during hemodialysis [43]. Recently, it was reported that PSS forms stable complexes with positively charged proteins that can be used in layer-by-layer assemblies to improve biological activity [44, 45].

In accord, the very high and opposite net charges of the two polymers (R-DPRs are positive, whereas PSS is negative) suggest a strong interaction between them. In fact, in a chemically similar arrangement, a picomolar Kd between two oppositely charged IDPs, histone H1 and prothymosin-α, was observed [34]. To address the Kd of the PSS - R-DPR interaction, we studied a whole range of PSS length variants from a monomer (PSS_1) to a 340-mer (PSS_340), as outlined in Scheme 1. To determine the Kd of PSS - R-DPR binding, we first studied a long PSS (PSS_43) and applied isothermal titration calorimetry (ITC), yielded very steep binding curves with both PR30 and GR30 (Fig. 1A, B), whereas PA30 which has no charge and is of limited toxicity in ALS/FTD models [46], gives no detectable heat signal (Fig. 1C). Analysis of PR30 and GR30 curves indicates very strong binding: fitting the data (Fig. 1D, E) yielded apparent Kd values of 12.6 nM and 2.4 nM for PR30 and GR30, respectively, but indicated no detectable binding of PA30 (Fig. 1F).

It is to be noted that numerous repetitions of this experiment yielded a binding constant in the range of nM to pM, and to obtain a valid binding constant in ITC, a “c factor” ($c = n[M]Kd$, where n is the binding stoichiometry, [M] the macromolecule concentration, and Kd the binding constant) must be between 10 and 100 [47]. Values of c that are too low (<10) can sometimes be used to fit Kd but cannot be used to accurately determine stoichiometry (n). Values of $c > 1000$ can be used to accurately determine n, but not Kd. Since binding stoichiometry in the PSS:R-DPR system is approximately 1 and PSS_43 concentration in the ITC cell is 20 µM, the c factor is 252,000 (Fig. 1D) and 48,000 (Fig. 1E), i.e., the accurate determination of Kd is probably beyond the limits of ITC. A further reduction of protein and ligand concentrations is not feasible since the signal-to-noise ratio becomes too low.

Therefore, to assess further the very strong interaction between PSS_43 and the R-DPRs, we implemented microscale thermophoresis (MST) measurements, in which fluorescently labelled PR30 and GR30 were titrated with PSS_43 (Suppl. Fig. S1). Here also, very steep binding curves were obtained for both DPRs. The obtained data analysed using the Hill-equation and resulted in strong binding constants 5.7 nM and 6.0 nM for PR30 and GR30, respectively.

We also applied fluorescence correlation spectroscopy (FCS) to analyze the binding of fluorescently labeled DPRs to PSS_43 and compared the deduced binding constants to those obtained using other techniques (ITC, MST) (Suppl. Fig. S2). In these experiments Kds were in the range of nanomolar; 5.2, 7.3, 9.3 nM based on rotational diffusion, fluorescence anisotropy and fluorescence life-time.

Given the very strong interaction with PSS_43, we next asked how the Kd changes with polymer length with PR30 (Fig. 1G) and GR30 (Fig. 4H). In both cases, the monomer and dimer show no measurable interaction, PSS_5 already binds with a Kd = 120 nM (PR30) and 150 nM (GR30), whereas longer variants bind significantly more tightly. PSS_22 has the full interaction strength, which varies a little with increasing length (Table 1, Fig. 1G, H). Given the expectation that PSS – R-DPR interaction is primarily driven by electrostatic attraction, we also carried out a salt titration of the PR30 – PSS_43 and GR30 – PSS_43 (Suppl. Fig. S3) system. As expected, the interaction is strongest at 0 mM NaCl, and becomes gradually weaker as salt is increased through 150 mM to 500 mM.

PSS inhibits the phase separation of R-DPRs

SGs involved in pathological protein aggregation in ALS/FTD contain proteins with domains that can undergo and drive LLPS. The most notable of these are RNA-binding domains (RNA recognition motifs, RRMs), and intrinsically disordered arginine-rich sequences (RGG boxes), which can also bind RNA or poly(ADP-ribose), initiate LLPS and lead eventually to the aggregation of prion-like domains [48-50]. It has been suggested that arginine-rich motifs can play a significant role in LLPS in both physiological and pathological processes [49, 50]. C9orf72-encoded R-DPRs have been linked with C9-ALS/FTD etiology [46], and suggested to exert their pathological effects primarily by impairing the formation of physiological nucleoli [17] and SGs [18]. In recent studies [17, 51, 52], it was suggested that R-DPR LLPS induced by crowding and RNA are reasonable approximations of the complex pathological processes, and thus we hypothesized that it provides a reasonable system for the initial assessment of the potential favorable effects of PSS variants in pathological situations.

Having established the very strong binding of PSS to R-DPRs (Fig. 1), we next asked if PSS inhibits the RNA-promoted LLPS of R-DPRs. We first initiated LLPS of the studied DPRs by four different RNA variants: polyU, polyA, tRNA and total RNA extracted from Neuro-2a cells (Fig. 2). By following LLPS by turbidity (OD 340 nm),

the signal of PR30 (Fig. 2A) and GR30 (Fig. 2B), but not PA30 (Fig. 2C) first increased rapidly, then slowly decreased, probably due to maturation (ripening) of droplets. This behaviour was typical for polyU and polyA, whereas relatively smaller turbidity values were observed for total RNA, suggesting the formation of bigger droplets. A different kinetic trajectory was recorded in the presence of tRNA, where, after a rapid increase, a slow decrease and rather constant OD value was observed. This behavior was consistent with earlier observations that LLPS is promoted by disordered (polyU, polyA), but not ordered (tRNA) RNA molecules [53].

We then studied the evolution of droplets by dynamic light scattering (DLS). For PR30 and GR30 (Fig. 2D, E) the droplets grew slowly, reaching a maximum in size (approximately 1-2 μm) in about 1h. In agreement with turbidity measurements, smaller droplets formed in the presence of tRNA for PR30 and GR30, whereas bigger droplets appeared in the presence of total RNA. Some difference was apparent between the two R-DPRs, as GR30 droplets showed slower growth than those formed of PR30. PA30, on the other hand, (Fig. 2F) showed no DLS signal, confirming the turbidity data proving the lack of LLPS in its case.

These conclusions were also confirmed by direct visualization of droplets by fluorescence microscopy (Figure 2G, H and I). Solutions of PR30 and GR30, but not of PA30, quickly formed many droplets upon the addition of all studied RNAs. Typically, the biggest ones appeared with total RNA and the smallest ones with tRNA, in accord with turbidity and DLS measurements. Overall, the results with the three different techniques agree that R-DPRs undergo LLPS in the presence of different RNAs, following somewhat different kinetic trajectories.

In pathological conditions, liquid droplets proceed toward aggregated states, as indicated by fluorescent indicators thioflavin T (ThT) or thioflavin S (ThS, in the presence of RNA [54, 55]). To address if the various R-DPR - RNA systems show this behavior, and thus can be considered as reasonable proxies to pathological LLPS mimicking C9-ALS/FTD processes we next followed the ThS fluorescence signal over 15h in different R-DPR – RNAs systems (Suppl. Fig. S4). PR30 and GR30, similarly to TAR DNA-binding protein 43 (TDP-43), a protein strongly implicated in the formation of pathological inclusions in ALS/FTD [56], developed intensive ThS signals with all RNA variants, polyU, polyA, tRNA, and total RNA (Suppl. Fig. S4A, B). PA30, which does not promote LLPS of R-DPRs, and is only moderately toxic in ALS/FTD models, did not show an increase in ThS fluorescence over an incubation of 15h.

Given the strong length dependence of PSS – R-DPR binding (Fig. 1, Table 1) and anticipating that the polymeric nature of PSS plays an important role in its effect on R-DPR LLPS, we first compared the influence of PSS_43 and sodium p-toluenesulfonate (monomer of PSS, cf. Scheme 1) on LLPS at identical monomer concentrations (i.e., applying PSS_1 at 43x concentration to that of PSS_43). We initiated LLPS of PR30 under these conditions by polyU and added PSS variants either before the initiation of LLPS or 30 min after polyU addition, following LLPS by turbidity (OD 340) (Fig. 2 K,

M) and DLS (Fig. 2L, N) measurements, also confirmed by microscopy (inserts). In all cases, strong interference of LLPS by polymeric PSS was observed. When PSS_43 (at a molar ratio of 1:1) was added to PR30 solution before polyU, it first resulted in rapid initial jump, followed by a slow rise in absorbance (Fig. 2K), which is opposite to the classical LLPS kinetic trajectory observed in the absence of PSS. DLS (Fig. 2L) showed the immediate formation of small condensates (around 200 nm, as opposed to 1-2 µm without PSS), which were stable over time. In bright-field microscopy (where 200 nm particles are too small to resolve) a small population of larger particles of about 1 µm in diameter was observed (inserts).

Monomeric PSS_1 applied at 43x the concentration of PSS_43 (Scheme 1A) had a basically different, although not negligible, effect: the increase and decrease in turbidity were slower than in the control experiment run without PSS. In accord, DLS measurements showed a significantly slower formation of droplets of approximately 800 nm in diameter (Fig. 2L), in between the size of droplets formed with and without PSS_43. This observation was fully supported by microscopy images (inserts) Moreover, on a different focusing plane, another population of big liquid-like structures was present, not detectable by DLS.

A similar set of experiments was performed for PR30 solutions in which PSS_43 or PSS_1 was added 30 min after the induction of LLPS (Fig. 2M, N). The polymer had an immediate, profound effect: it reversed the direction of turbidity change, resulting in a slow increase in turbidity to a constant value of about 0.4 (Fig. 2M). DLS measurements revealed an immediate cessation of the growing of droplets and their dispersion to small ones of about 200 nm in diameter (Fig. 2N). Microscopy images show only a few small droplets whose size was either too high or their concentration was too low to be detected by DLS (inserts).

When the monomer PSS_1 was added to an already phase-separating solution of PR30, it hardly affected the turbidity signal. DLS showed a drop in droplet size, to around 800-1000 nm, confirming an effect that is much less than that of PSS_43. Microscopy also supported this conclusion: droplets of µm size are observed together with big, apparently liquid structures detectable in a different focusing plane.

As very similar behavior was observed for the GR30 solution (Suppl. Fig. S5), we concluded that polymeric PSS has a dramatic effect on the LLPS propensity of R-DPRs. In this, the polymeric nature of PSS is of utmost importance, as the application of the same number of units in the form of a monomer has much less effect.

Given the importance of polymer length in R-DPR binding (Fig. 1) and in potential applications against R-DPR toxicity, we next scanned the whole range of PSS variants (cf. Scheme 1) for their inhibitory effect of R-DPR LLPS. In these experiments (Fig. 3), LLPS of PR30 or GR30 was initiated by polyU, and PSS length variants (always at concentrations to ensure a PSS unit to DPR ratio 1:1) were added before or after the initiation of LLPS (adding polyU) and LLPS was quantitated by the maximal value of

its OD340 turbidity curve (as on Fig. 2A and B). When the polymer was added before LLPS, the critical length for inhibition is between n = 5 and 22 with both R-DPRs (Fig. 3A, C). When the PSS is added after LLPS, there is no apparent effect (Fig. 3E, G), but it has to be considered that turbidity is not a good indicator of LLPS inhibition (cf. Fig. 2). When measured by DLS, even a PSS monomer had a significant effect in all scenarios (whether with PR30 or GR30, added before or after polyU), and the full effect is reached at n = 22 (reducing droplets to about 1/5 of their original size), above which increasing polymer length had no further effect (Fig. 3B, D, F, H). Microscopic images support this conclusion (Fig. 3, inserts), although they cannot be as well quantified and are complicated by the occasional appearance of much larger condensates. In all, the length n = 22 is close to the length of DPRs (n = 30), which may be of importance in reaching a maximal effect, serving as a guide in our further quest for PSS variant(s) most effective in countering R-DPR toxicity.

PSS releases tightly bound RNA from R-DPRs

To help mechanistically interpret the observed strong effect of PSS on the RNA-induced LLPS of R-DPRs elicited by their very strong binding, we carried out electrophoretic mobility shift assays (EMSA) experiments with the R-DPR – RNA – PSS system. In particular, we addressed if RNA bound by R-DPRs can be released by PSS due to a tighter PSS – R-DPR than RNA – R-DPR interaction. To determine first the Kd of RNA – R-DPR interaction, we titrated 32P-labelled mRNA with either PR30 (Fig. 4A, B) or GR30 (Fig. 4C, D), and determined the amount of unbound and bound RNA by densitometry following autoradiography of the unbound (lower apparent Mw) and R-DPR-bound (higher apparent Mw) RNA bands. Fitting the titration curves by a 1:1 binding model, we obtained the Kd for RNA-PR30 (125 nM) and RNA-GR30 (70 nM) interaction; apparently, they are almost two orders of magnitude weaker than the respective interactions of PSS binding to R-DPRs.

We then asked how the amplitude of LLPS, as measured by peak turbidity (cf. Fig. 1), changes upon titration of R-DPRs with an excess of RNA. In the case of both PR30 (Fig. 4E) and GR30 (Fig. 4G), LLPS shows a reentrant behavior [57, 58], increasing initially but being fully inhibited at the excess of RNA, which is in line with a model assuming optimal LLPS at stoichiometric amounts of the two oppositely charged components. In fact, when LLPS intensity curves are plotted as a function of the charge ratio of RNA vs. DPRs, the maximum of LLPS is achieved in both cases (Fig. 4F, H) at 1:1 charge ratio, above which LLPS becomes inhibited by excess RNA (and dominance of its negative charge).

LLPS of R-DPRs is promoted by RNA [51], which probably acts by establishing crosslinks between R-DPR – RNA clusters, as observed for the LLPS of G3BP1 [59]. In this scenario the tighter binding of PSS to R-DPRs might suggest that the inhibition of RNA-driven LLPS stems from releasing RNA from R-DPRs. Therefore, we next

asked if PSS added to the RNA - R-DPR mixture can liberate RNA from the complex. As RNA binds very tightly to R-DPRs, resulting in its apparently very slow release from the complex and equilibration with PSS, we first mixed PSS_43 and RNA at equimolar concentrations, and then added R-DPRs PR30 (Fig. 4I) and GR30 (Fig. 4J) in increasing concentrations. RNA appeared in isolation every time PSS_43 was in molar excess to the R-DPR, with the RNA-DPR complex appearing on the gel only in the absence of PSS.

These results support the model that the inhibitory effect of PSS on RNA - R-DPR LLPS emerges from PSS terminating RNA binding, while not being able to promote a PSS - R-DPR phase separation. This is not evident, as R-DPR – PSS droplets could form similarly to R-DPR – RNA droplets, due to similar charge complementarity in the two systems. Whereas DLS and microscopy experiments (Fig. 2) suggest that this is not the case, we have further approached this issue by fluorescence recovery after photobleaching (FRAP) experiments, which can give direct information on the dynamics of condensates. In fact, when measuring the FRAP recovery of R-DPR - polyU droplets, they appear fully mobile, underscoring their liquid nature compatible with a model of formation by LLPS (Fig. 4K - N). When PSS of different length is added, whether before or after initiating LLPS (causing the appearance of much smaller droplets, cf. Fig. 2 and Fig. 3), an interesting trend appears: at lengths PSS_1 to PSS_2, which have an overall smaller effect, the droplets are fully mobile, suggesting little interference by PSS. At PSS_5, and then fully from PSS_22, droplets become very rigid, their fraction of recovery dropping to about 30% or less. This means that longer PSS variants not only inhibit LLPS and affect droplet morphology to a great extent, they also basically reduce the dynamics of droplets (condensates) that replace liquid droplets.

Molecular mechanisms of R-DPR – PSS interaction

These results suggest not only that PSS can engage in much stronger interactions with R-DPRs than RNA, but also that in an atomistic-structural sense these interactions critically differ so that not even the very long PSS_340 (Fig. 5K-N) can support the formation of liquid droplets. To understand this special mode of interaction in atomistic detail, we carried out experiments and modelling to characterize the R-DPR – PSS interaction. First, we applied NMR spectroscopy to characterize which regions of the polymers engage in contacts upon interaction. As both R-DPRs and PSS are highly repetitive, causing severe signal overlap in multi-dimensional NMR, we recorded 1D 1H NMR spectra of PSS_43 and PR30 (Fig. 5A, B) and GR30 and PA30 (Suppl. Fig. S6). The spectra of all three DPRs were then also acquired in the presence of increasing concentrations of PSS_43.

The spectrum of PR30 has a peak in the amide region at 8.4 ppm. The addition of 10 µM PSS_43 results in a decrease of intensity of this peak, whereas at 70 µM PSS the

amide peak completely disappears and the intensity of the PSS_43 peak starts to increase. The peaks of PSS appear at 7.4 and 6.6 ppm, corresponding to the aromatic ring of PSS [60]. In the aliphatic region, multiple peaks for PR30 resulting from spin-spin coupling can be observed. Upon the addition of PSS, a similar binding behaviour was observed as in the amide region, the intensity of the backbone of PSS_43 [60] starts to appear above about 70 µM PSS. The interaction of PSS_43 and PR30 is based on a slow exchange of protons; this data was fitted with 1:1 binding, because tight binding fitting did not result in reliable dissociation constant (Fig. 5B-D).

In the case of GR30, two peaks appear in the amide region, at 8.6 and 8.35 ppm. Their intensity decreases upon the addition of 10 µM PSS_43, and the peaks completely disappear at 100 µM PSS_43. The data were fitted by 1:1 binding, because slow-exchange fitting did not result in a reliable dissociation constant (Suppl. Fig. S6AE-C).

In the case of PA30, a peak in the amide region was observed at 8.2 ppm, which decreases upon the addition of 20 µM PSS_43, upon further addition of PSS_43, it starts to decrease. We can conclude that the interaction is weak and is based on a fast exchange, with multiple binding events involved in the interaction between PSS and PA30 (Suppl. Fig. S6D-F).

Overall, the interaction between R-DPRs is based on a slow exchange, whereas the interaction of PSS_43 and PA30 is based on a fast exchange that involves multiple binding events. With PR30 and GR30, both the backbone (amide region) and side chains (aliphatic region) are involved in binding.

As NMR cannot provide high-resolution structural information for the R-DPR – PS interaction, we carried out all-atom molecular dynamics (MD) simulations to characterize the system further. First, single molecules, i.e., PSS_20, GR10, PR10, and PA10 (for feasibility, DPRs shorter than n = 30 were modeled) were equilibrated and analyzed. The obtained conformations and secondary structure evolutions are presented in the Suppl. material (Suppl. Figs. S7-S10). These configurations were used further to construct multiple-molecule systems, i.e., containing PSS and peptide pairs (1:1 system) and more complex mixtures containing 7 copies of each molecule (7:7 system). The MD behavior of the multi-molecule systems is outlined in Fig. 5, and Suppl. Figs. S11-S19, and Suppl. Tables S2 and S3.

The MD results highlight significant differences between R-DPRs GR10 (Fig. 5E) and PR10 (Fig. 5F), which show strong association with PSS20, and PA10 (Fig. 5G) which engages only in very weak/transient interactions with the charged polymer. The interaction between these peptides and PSS leads to the release of counterions condensed around the PSS molecule, which is manifested by the decrease in the peak height of radial distribution function (RDF) between the S atoms and Na+ ions (Fig. 8H): such an effect is suggestive of a primarily electrostatic component driving poly-PR – PSS and poly-GR – PSS interactions, as already suggested for polyelectrolyte complex formation [61], and supported by the salt dependence of their PSS_43

binding (Suppl. Fig. S3). PSS also forms a hydrogen-bond network with GR10 and PR10 (Suppl. Tables S2 and S3), which is more extensive than the one with PA10.

MD simulations of multicomponent (7:7) systems (Figs. 5I-L) confirm these predictions of atomic contacts observed in the 1:1 systems and underscore the different LLPS tendencies of R-DPRs (cf. Fig. 2). That is, both GR10 (Fig. 5I) and PR10 (Fig. 5J), but not PA10 (Fig. 5K), form dense clusters with PSS, quantitatively confirmed by RDF values between Cα atoms of DPRs and sulfur atoms of PSS (Fig. 5L). This behavior is in line with the observed formation of small residual clusters from R-DPR – RNA droplets upon the addition of PSS (Fig. 2), as also underscored by their reduced dynamics observed by FRAP (Fig. 4).

MD simulations can further assess the electrostatic component of interactions, as simulations at different salt concentrations can be compared. A strong salt effect upon varying NaCl concentration appears (Figs. 5E-L show results of 150 mM NaCl concentration; results of higher salt are shown in Suppl. Fig. S11). RDFs indicate that the release of counterions condensed around PSS is significantly weaker at higher NaCl concentrations, with a similar trend observable for hydrogen bonding (Suppl. Table S2) and the number of contacts between the peptides and PSS (Suppl. Fig. S19), all these trends underscore the primarily electrostatic nature of interactions.

To provide further experimental confirmation of these inferences, we have carried out salt titrations of R-DPR – PSS interaction by ITC and salt and 1,6-hexanediol titration of R-DPR – RNA LLPS by turbidimetry. In both systems, salt has a strong inhibitory effect on LLPS of both PR30 and GR30, even at physiological, 150 mM concentration. Interestingly, 1,6-hexanediol, an agent known to interfere with hydrophobic interactions, is hardly effective at 150 mM NaCl, suggesting that electrostatics is the dominant force in R-DPR LLPS, hydrophobicity playing a secondary role.

PSS is of limited cell toxicity and can penetrate cells

Motivated by the very effective inhibition of the LLPS of R-DPRs by PSS, we wanted to move toward cellular applications of the polymer, in particular to testing if it can avert R-DPR-induced toxicity. To this end, we first asked if PSS itself is toxic to cells. It is to be remembered that it is taken at very high doses in hyperkalemia [35, 36], when it may not reach cells, though.

First, we incubated Neuro 2a cells with all different PSS length variants (from n = 1 to 340) for 24h and assessed cell viability by total ATP content (Fig. 6A). We found that with the exception of the longest, PSS_340 (IC50 = 5.3 ± 6.8 μM), none of the other PSS variants is toxic. In comparison, we have also incubated Neuro 2a cells with the three dipeptide repeats (Fig. 6B), and found that GR30 (IC50 = 4.9 ± 2.4 μM) and PR30 (IC50 = 12.8 ± 7.7 μM) are highly toxic, whereas PA30 has a very moderate effect on cells (IC50 > 30 μM), in accord with similar experiments carried out on

different cell lines in the literature [62, 63]. Whereas R-DPRs are known to be cell penetrable [17, 64], it has never been tested if PSS could penetrate the cell membrane engage with R-DPRs within cells. To this end, we tested two types of cells by fluorescent microscopy, adding fluorescently labelled PSS_73*_Rhod (a heterogeneous mixture), PSS_5_Rhod and PSS_ 24_Rhod (cf. Scheme 1) to Neuro 2a cells (Fig. 6C), and PSS_73*_Rhod and PSS_43_Rhod to U2OS cells (Fig. 6D). Images taken after 24 h incubation show the intracellular localization of all PSS variants in both cells. When we compared the localization of PSS_73*_Rhod and DyLight 488-labelled GR30 or PR30 inside cells (Fig. 6E), we observed the colocalization of R-DPR and PSS molecules. 4,6-Diamidino2-phenylindole (DAPI) staining for DNA showed a preferential cytoplasmic localization of both PSS and DPR molecules. Earlier, it was shown that while PR30 is predominantly localized in the nucleus, GR30 is found in both the nucleus and the cytoplasm [64]. Apparently, when PSS is also present, it changes the preferential localization of both R-DPRs to the cytoplasm (Fig. 6E), which implies their physical association in cells. This, given the lack of PSS-driven R-DPR LLPS (Fig. 2M and Fig. NL, N), raises hopes that PSS can counter R-DPR toxicity in cells. We addressed this next.

PSS is a strong inhibitor of cellular R-DPR toxicity

Motivated by its very tight R-DPR binding, efficient LLPS inhibition, lack of cell toxicity, cell penetration and cellular colocalization with R-DPRs, we next studied the effect of PSS on cell toxicity of R-DPRs. We have already shown that both PR30 and GR30 are very toxic to cells measured by total ATP content (Fig. 6B), and here we also observe that they cause profound changes in the morphology of Neuro 2a cells and decrease the total number of cells in cell culture (Fig. 7A, B). Also in accord with ATP content measurements, GR30 is more toxic than PR30, whereas PA30 is not toxic to cells.

Most importantly, the toxicity of R-DPRs is reversed by PSS. When Neuro 2a cells were incubated with PR30 or GR30 at different concentrations, together with 20 or 200 μM PSS_1, we see very little cell protection (Fig. 7C). PSS_5, on the other hand, is already very effective at 200 μM concentration (Fig. 7D), whereas upon the application of only 20 μM of the longer PSS_22 and PSS_43, the total ATP content measured after 24 h incubation shows a diminution of R-DPR toxicity, i.e., a significant increase in the effective IC50 values of R-DPRs (to 36.47 ± 6.7 μM (PSS_22) and 42.1 ± 10.4 μM (PSS_43) in the case of PR30, and 9.0 ± 3.1 μM (PSS_43) in the case of GR30 (Fig. 7E, F, G). A similar experiment was performed with PA30, where no effect was observed in presence of PSS_43 (Fig. 7H).

These effects are not unexpected, given the very tight binding of PSS to R-DPRs, which probably precludes their entry into cells. This experiment, however, does not adequately model the disease situation, in which DPRs would be synthesized within

cells, while PSS is administered from outside. To model this disease situation better, we preincubated cells with 10 μM PR30 (for the times indicated, when R-DPRs enter cells, Fig. 6I), then cells were washed to remove the DPR and PSS_43 at 10 μM was added. Following further 48h of incubation, the total ATP content of cells (Fig. 7I) showed that cells were affected by toxic PR30, but the ones incubated with PR30 for a longer period (20-30h) were saved by PSS_43, even though PSS and the DPR were never in physical contact outside the cell. This observation can be rationalized by two scenarios, either that (i) PR30 can equilibrate through the cell membrane and is effectively dragged out of cells by external PSS, or (ii) PSS penetrates the cell membrane and physically encounters the toxic R-DPR inside cells. To address these possibilities, cells were also preincubated with 10 μM PSS_43 for 2h (when it enters cells cf. Fig. 6), then PR30 at the concentrations indicated was added, and ATP content measured, after 24 h incubation (Fig. 7J). Clearly, cells after long incubations experienced much less toxicity, attesting to the protective effect of PSS.

PSS protects zebrafish embryos against DPR toxicity

We also aimed to demonstrate that PSS added externally can not only protect against R-DPR toxicity in cellular systems, but also in an animal model. To this end, we have carried out zebrafish experiments, in which we first asked whether PSS is taken up by zebrafish embryos. To assess if this is the case, zebrafish embryos were incubated with PSS_ 43_Rhod and PSS_340_Rhod at 6h post-fertilization (hpf) for 24 hr (embryos at 6 hpf called “gastrula”). At 30 hpf, embryos were imaged with confocal microscopy (Fig. 8A) to visualize the localization of PSS. As seen, PSS_340_Rhod is spread homogeneously while PSS_ 43 is heterogeneously distributed and forms puncta in the whole embryo, including its head and tail. Based on this observation, PSS can apparently cross the outer membrane and enter the embryo.

We then wanted to obtain a toxicity profile of all different variants of PSS (from PSS_1 to PSS_ 340, cf. Scheme 1), at concentrations spanning from 30 μM to 500 μM, over a time course of up to 48 hr. Toxicity was assessed by observing the extent of chorion collapse caused by PSS (embryos of normal and collapsed chorion are shown in Fig. 8 B). We found that none of the PSS variants are toxic at 250 μM, except for PSS_340, which causes chorion damage at this concentration (Fig. 8C, data for other concentrations between 30 to 500 μM are represented in Suppl. Fig. S20A-D). This behavior resembles the toxicity profile observed with Neuro 2a cells (Fig. 6). Since PSS is not toxic in the presence of a chorion, we also incubated dechorionated embryos with PSS_22 and PSS_43 for 24 h, starting at the gastrula stage, with concentrations up to 250 μM (Fig. 8D). We found that neither PSS_22 nor PSS_43 is toxic at concentrations 32.25 μM or below.

Subsequently, to assess R-DPR toxicity and potential protection by PSS, we set up an assay to measure axonal length by using Synaptic vesicle 2 protein (SV2) staining

as a marker, as described [65]. A plasmid encoding for PR50 was injected in the yolk sac of the zebrafish embryo at the 1-2-cell stage, to enable the translation of the polypeptide, and the axonal parameter was measured at 30 hpf. The DPR significantly decreased axon length (Fig. 8E). Next, the same assay was repeated by incubating the embryos in the presence of PSS_43 added at 15 mM concentration. PSS_43 significantly inhibits the effect of PR50, practically recovering axon length to its level observed without the R-DPR expression (Fig. 8E).

Limited mouse toxicity of PSS

Mouse toxicity analysis of PSS_22 upon intracerebroventricular (ICV) injection was assessed at 1 mM and 10 mM concentrations. A toxicity score was given by assessing weight (loss), seizure, atypical behaviour, hyperactivity, and normal grooming/eating of 5 mice at each concentration.

The results showed that mice injected with phosphate-buffered saline (PBS) vehicle and 1 mM PSS_22 did not exhibit weight loss during a 7-day follow-up period and their toxicity score did not exceed 1 on a scale of 50, indicating that 1 mM PSS_22 injection is safe for a one-week period. On the other hand, mice injected with 10 mM PSS exhibited signs of toxicity with a mean score of 44.8 directly after the surgery. These results suggest a safe ICV application window of PSS_22 up to 1 mM in mouse, which sets the stage for future protection and efficacy studies.

Discussion

Neurodegenerative diseases, such as Alzheimer's disease, Parkinson's disease or ALS/FTD represent an almost unbearable burden on our ageing society, against which we have only very limited medical tools so far. We can mostly resort to symptomatic treatment to delay the progression of the disease (most effective in Parkinson's disease). A special challenge with ALS/FTD is that it is a very rapidly progressing disease, leading to death within 2-5 years after diagnosis [4, 66, 67]. A recent, inspiring breakthrough of the field is that Tofersen, an ASO against SOD1-ALS/FTD [27]has been recently approved by FDA, while an ASO against C9orf72 mRNA has reached clinical trials [28-30]. More help is unquestionably needed, in which PSS may bring a long-awaited breakthrough, coming from a truly unexpected chemical angle.

C9orf72 R-DPRs are thought to be the primary culprots in neuronal cell death in C9-ALS/FTD [17, 56, 68], and have been shown to be highly toxic in cellular [65, 69] and animal [65, 70-72] models of the disease. Their mechanism of action is not fully clear, but impairment of LLPS processes leading to the disruption of cellular RNA metabolism and the dynamics of ribonucleoprotein condensates, such as SGs and nucleoli, appear to play a critical role [14-16]. Due to their high arginine content, poly-

PR and poly-GR can actually penetrate the cell membrane and be toxic to cells when added externally [16, 17].

Whereas due to their central role in C9-ALS/FTD, these R-DPRs are potentially very valuable drug targets [28-30], due to their intrinsically disordered, extremely non-natural character as proteins, they are considered mostly undruggable and have not yet been the subject of rational drug development efforts. Our results with PSS may turn this situation around. In every relevant aspect, we have observed its high potential, as it can: (i) bind R-DPRs very tightly, (ii) release their bound RNAs, (iii) inhibit R-DPR LLPS, (iv) enter cells on its own, while (v) having limited toxicity. Most importantly, (vi) it curbs R-DPR toxicity in cells and even in an animal model.

Of course, although we have made a broad range of relevant observations, the cellular mechanism(s) of PSS protection needs further scrutiny, as it may act in various ways. As demonstrated, the most toxic R-DPRs (poly-PR and poly-GR) are cell penetrable, which may suggest that they can equilibrate across cell membranes. Of course, very tight RNA binding tends to keep DPRs inside cells. However, if an even more potent binder, PSS, is added in the extracellular space, it may alter this equilibrium and cause a net outflow of DPRs from cells, thus reducing their toxic load in the disease. Another possibility is that - as we have shown – PSS can enter cells, co-localize with R-DPRs, reduce their effective intracellular concentration and/or alter their RNA binding and LLPS propensity, while not promoting R-DPR – PSS LLPS on its own.

The observation that PSS can effectively co–nter LLPS of DPRs, nevertheless, may strike at the very heart of the pathogenic mechanism, which may stem from affecting the balanced formation and dispersion of cellular ribonucleoprotein condensates, such as SGs and nucleoli [14-16], in affected cells under physiological conditions. We can anticipate that it is central to PSS efficacy that the polymer actually binds R-DPRs much tighter than RNA, thus it can favorably compete with pathogenic mechanisms realized through R-DPR – RNA interactions, and possibly evigorated impaired RNA metabolism, such as splicing, translation, transport and condensation.

A special aspect of the use of PSS is that it is an FDA-approved drug [42, 73], so its repurposing for C9orf72-related ALS/FTD cases represents a highly appealing opportunity to develop an effective drug. It was approved in 1958 [73], and has since been used broadly, in a variety of products (Suppl. Table S1). Its successful targeting R-DPRs as a novel modality of countering C9-ALS/FTD is validated by recent progress of anti-C9orf72 mRNA ASOs, which decrease R-DPR expression and entered clinical triels [28-30].

It is not to be left without consideration that PSS can be toxic upon particular ways of administration, which may need to be further worked out, as its penetration of the blood-brain barrier (BBB) has never been tested and assessed. Our results pointing to limited toxicity in cells, a zebrafish model and even in mice, are encouraging for further pre-clinical animal studies. As an additional twist in the tale, it is of specific

interest that toxic R-DPRs are involved not only in ALS/FTD but also other diseases induced by repeat expansions. To mention a few, poly-PR is involved in spinocerebellar ataxia type 36 (SCA36) [74], poly-GR in X-linked dystonia parkinsonism (XDP) [75], and poly-QAGR in myotonic dystrophy type 2 (DM2) [76], while toxicity of highly positively charged proteins and peptides ahs been noted in a broad range of infections and diseases, considered as “polycationic poisoning” [77]. The potential application of PSS as a remedy, therefore, may also be tried in these other indications.

Materials and Methods

Chemical reagents

Sodium p-toluenesulfonate (PSS monomer, cf. Scheme 1), 95%, and poly(sodium 4-styrenesulfonate), PSS Mw = 70 000 (PSS_340) were purchased from Sigma Aldrich while PSS of Mw = 1 000 (PSS_5) and Mw = 8 890 (Mw/Mn = 1.09) (PSS_43) were bought from Polysciences and Scientific Polymer Products Inc., respectively. Rhodamine-labelled PSS (heterogeneous mixture of an average Mw = 15 000) was bought from Surflay Nanotec. HEPES, Tris buffers, NaCl Tween-20, EDTA N,N,N′,N′-Tetramethyl ethylenediamine (TEMED) were purchased from Aldrich. Boric acid and ammonium persulfate (APS) were bought from VWR company while Acrylamide from BioRad.

Peptides and RNAs

PR30, GR30 and PA30 dipeptide repeats were synthesised by Synpeptide Co., Ltd company, Shanghai, China. Polyuridylic acid (PolyU, cat. no. P9528) potassium salt a heterogeneous and Polyadenylic acid (PolyA, cat. no. P9403) with molar mass ranging between 700-3500 kDa were purchased from Sigma Aldrich. Yeast tRNA (tRNA) was purchased from Thermo Scientific (cat. no. 15401011). Total RNA was extracted from Neuro 2a cells using Trizol from Fisher Scientific, (cat. no.15-596-026) and accompanying protocol.

Liquid-liquid phase separation (LLPS)

Liquid-liquid phase separation (LLPS) of C9orf72 DPRs was initiated in a buffer of 10 mM HEPES, pH 7.4, at various NaCl concentrations (0 mM, 50 mM and 150 mM). The concentration of DPRs varied from 10 µM to 80 µM, whereas the concentration of RNAs varied from 0.05 to 0.8 µg/µl. LLPS was induced by the addition of RNA and was followed by either turbidity measurements or dynamic light scattering (DLS).

Turbidity measurements

LLPS was followed by monitoring the change of the turbidity of the solution in a BioTek SynergyTM Mx plate reader in which non-binding black 96 well plates with transparent bottoms (Sigma®) were used. Solutions were mixed, the plate covered with a transparent film (VIEWsealTM), and the absorbance of the solution was monitored at 340 nm for 2 hours at 25°C with continuous shaking. The experiments were conducted in triplicate and then averaged.

Dynamic light scattering (DLS)

Dynamic light scattering (DLS) measurements were carried out on a DynaPro NanoStar (Wyatt) instrument. A disposable cuvette (WYATT technology) was filled with 50 µl of DPR solution with different types of RNA, under the same conditions used in turbidity measurements. The sides of the cuvette were filled with water and a cap was put on top. The intensity of scattered light was recorded at a scattering angle of 95° at 25°C for a period of 2 hours, collecting 7 acquisitions (8 s each). Each measurement was repeated at least 3 times. The software package DYNAMICS 7.1.9 was used for data analysis.

Fluorescent labelling with Dylight® 488

100 µM of Dylight® 488 dye (Thermo Fisher Scientific) was used to label DPRs (PR30, GR30 and PA30) for fluorescence microscopy measurements. 50 µM of each DPR was dissolved in the reaction buffer (1x PBS, 10 mM MgCl2, 0.05% Tween 20), the dye added and then the solution incubated at room temperature for 30 min in darkness. The mixture was then desalted with a Pierce™ Peptide Desalting Spin Column (Thermo Fisher Scientific). Fluorescently labelled DPRs were protected from light and stored at -80°C.

Fluorescent and brightfield microscopy

Microscopy measurements were carried out on a Leica DMi8 microscope. To reach appropriate fluorescence intensities, Dylight® 488-labeled DPRs were mixed with the same, but non-labelled, peptides (at a 1:200 ratio). Then, phase separation was induced by the addition of the desired amount of RNAs. The solution was incubated at 25°C and droplets were visualized with 100x magnification with brightfield, and/or fluorescence microscopy (FITC filter).

Microscopy

The response of Neuro 2a cells to DPR and/or PSS treatment was also monitored by direct microscopic imaging. To this end, cells were plated in 24-well cell culture plates (Greiner Bio One) at a cell density of 0.1 x 106, to which DPR and/or PSS solution at the appropriate concentrations were added the following day. After 24 hours, microscopic images were recorded on a Leica DMi8 microscope equipped with a Leica DFC7000 GT camera with a10x objective. Cell viability was evaluated by counting the cells. Data were normalized to untreated cells imaged without added compounds.

Isothermal titration calorimetry (ITC)

ITC experiments were carried out on a MicroCal iTC200 system. For each measurement PR30, GR30, PA30 and PSS samples were dialyzed overnight into 10 mM HEPES, 50 mM NaCl, pH 7.4 buffer at various NaCl concentrations (50 mM, 150 mM or 500 mM). The PSS solution was filled in the ITC cell, the actual DPR into the syringe, from where it was injected into the cell in a series of 2 µl aliquots at 25°C, to reach the final concentrations indicated in figure legends. The raw ITC data were fitted to a single binding site model by the MicroCal PEAQ-ITC Analysis Software provided by the manufacturer.

Microscale Thermophoresis (MST)

MST measurements were performed on a Monolith NT.115 instrument from NanoTemper accompanied with Nano Temper Control 1.1.9 software at room temperature. Premium capillaries (MonolithTM NT.115 Series) from NanoTemper company and MST-binding buffer (10 mM HEPES, pH 7.4, 150 mM NaCl, 0.05 % Tween) were used for all experiments. DPRs (PR30, GR30 and PA30) were labelled by the Protein Labeling Kit, Red-NHS, 2nd generation (Cat. No. MO-L011) - amine reactive from NanoTemper according to the protocol provided. MST data were analysed by either the NanoTemper Analysis 1.2.101 software or GraphPad Prism. In either case the data were fitted with the Hill equation, with the Hill coefficient constrained to 1, i.e., by assuming a binding stoichiometry of 1:1. Each experiment was technically repeated at least three or more times and the mean half effective concentration (logIC50) values were calculated with standard error (SE).

Electrophoretic mobility shift assay (EMSA)

32P-labelled mRNA from Sulfolobus acidocaldarius (5'UTR region + piece of 5'end of the ORF), with a total length of 109 ntb was prepared by 5′-end-labelling using [γ-32P]-ATP (Perkin Elmer) and T4 polynucleotide kinase (Thermo Scientific) followed by

dephosphorylation using FastAP thermosensitive alkaline phosphatase from Thermo Scientific. Labelled mRNA fragments were subsequently purified using MEGAclear™ Kit (Thermo Fisher Scientific). EMSA experiments were performed with approximately 0.1 nM 32P-labelled mRNA and concentration of PR30 and GR30 ranging from 10 to 260 nM. Binding reactions of mRNA and R-DPRs and PSS_43 was prepared in buffer composed of 10 mM HEPES, 150 mM NaCl, pH 7.4 and allowed to equilibrate at 37 °C prior to electrophoresis on 6% acrylamide gels in TEB buffer (89 mM TRIS, 2.5 mM EDTA, and 89 mM boric acid).

Molecular dynamics (MD) simulations

The all-atom molecular dynamics (MD) simulation of PSS_20 and PR10, GR10 and PA10 systems were performed with the Gromacs 2019.2 package [78-80]. The OPLS-aa force field [81] was used, as it was proved to be a right choice for both peptides [82, 83] and PSS molecule [84, 85]. Sodium and chloride ions were modelled using parameters from [86] and [87], respectively. The explicit TIP4P model was employed for water [88].

Simulations were run at three different salt concentrations (50 mM, 150 mM and 500 mM NaCl). The first step involved a single-molecule equilibration in a given salt concentration. After solvation and ion addition, the system was energy minimized and a 0.1 ns NVT equilibration was performed. The DPR peptides and the PSS molecules were then simulated in an NPT ensemble for 300 and 100 ns, respectively. For each DPR, three different initial configurations were simulated. The obtained molecule conformations were further used for the simulations of 1 PSS_20 - 1 DPR (1:1) and 7 PSS_20 - 7 DPR (7:7) systems (having 1 or 7 of both types of molecules in the simulation box). The initial configurations for these systems were constructed by placing one (for 1:1) or seven (for 7:7) copies of each final configuration of the single molecule MD simulations in a random position and orientation in a simulation box of (9 nm)3 for the 1:1 or (15.0 nm)3 for the 7:7 systems. The systems obtained were simulated in an NPT ensemble for 250 ns. The convergence of the number of contacts between PSS and peptides was used as an indicator for the system equilibration (Suppl. Fig. S12) and the analysis was done for the last 50 ns.

In all simulations, the approach described in [89] was used to control the temperature while the Parrinello–Rahman algorithm was used for the barostat [90], where the time constants were 0.5 ps and 2 ps, respectively. The temperature and the system pressure were set to 298 K and 1 bar, respectively. The long-range electrostatic interactions were calculated using the PME method [91] while the van der Waals interactions were described using the Lennard-Jones potential and a 1.0 nm cut-off. LINCS [92] algorithm constrain the bonds between H and heavy atoms in the PSS and peptide molecules, while for water molecules the SETTLE algorithm [93] was used. A

2-fs time step was used for integrating the equations of motion. VMD software has been used for visualizations [94].

NMR

PSS-DPR interactions were also monitored by nuclear magnetic resonance (NMR) on a Varian INOVA 800 MHz spectrometer equipped with a Bruker console and cryo-probe head. Data processing was performed using Topspin v. 4, and data was plotted by GraphPad Prism and Topspin v.4. The sample buffer was 50 mM sodium phosphate, 50 mM NaCl, pH 7.0 and 5 % D2O.

Cell culture

Neuro-2a from cell line service (CLS), and U2OS cell lines were maintained in Dulbecco's modified Eagle's medium (DMEM, Gibco) supplemented with 10% FBS and 1% penicillin/streptavidin (Gibco) at 37oC in a humidified incubator with 10% CO2.

Assaying cellular ATP content

To assess changes in cell viability, we measured the ATP content of Neuro 2a cells. To this end, cells were seeded in white transparent-bottom 96 well microplates from life sciences research (Perkin Elmer) at 20,000 cells per well and incubated at 37°C with 5% CO2 overnight. The medium was carefully removed, PSS at the appropriate concentration was added to the wells, and the plate was then incubated for 24 hours. The ATP content was measured at various time points by ATPlite Luminescence Assay System (PerkinELmer). Luminescence was measured by the BioTek SynergyTM Mx plate reader. The luminescence of cells without added compounds was taken as 100%.

Zebrafish experiments

AB strains of zebrafish were injected at 1-2 cell stages in a yolk sac with different RNA. Injected embryos were incubated at 28 °C and after 6 hpf embryos were dechorionated using forceps and PSS was added at the indicated concentration. Morphologically normal embryos were deyolked manually and fixed with 4% formaldehyde at 4 °C in phosphate-buffered saline (PBS). Embryo s were permeabilized with acetone for 1h at -20 °C, blocked with 1 %BSA/ 1%DMSO/PBS for 1 hr at room temperature and immunostained with mouse anti-SV2 AB2315387 and secondary Alexa Fluor 555 anti-mouse antibody from Molecular probes, Eugene.

Phenotyping was performed with 15 consecutive embryos per condition by imaging with Leica DM 3000 LED microscope using Lucia software. For axonal lengths, five predefined and consecutive motor axons from 8th to 17th axon on both sides. GFP encoding RNA was used to control these experiments.

Mouse toxicity

Mouse toxicity analysis was carried out by Neuro-Sys Vivo SAS (Gardanne, France). The aim of the study was to administer PSS_22 in the brain of 12-week-old adult male C57BL/6 mice (by intracerebroventricular (ICV) injection), to evaluate its potential acute toxicity. Mice were monitored (body mass, daily observation) for 7 days.

PSS_22 was injected in 5 µl volume in sterile PBS as carrier, at either 1 mM or 10 mM concentration (5 mice each), and a toxicity score was given based on assessing: seizure, atypical behaviour, hyperactivity, normal grooming/eating.

Abbreviations

ALS: amyotrophic lateral sclerosis; APS: ammonium persulfate; ASO: antisense oligonucleotide; BBB: blood-brain barrier; BLI: bio-layer interferometry; DAPI: 4,6-diamidino2-phenylindole; DLS: dynamic light scattering; DPR: dipeptide repeat; EMSA: electrophoretic mobility shift assay; fALS: familial amyotrophic lateral sclerosis; FDA: Food and Drug Administration; FRAP: fluorescence recovery after photobleaching; FTD: frontotemporal dementia; FUS: fused in sarcoma; G3BP1/2: Ras GTPase-activating protein-binding protein 1/2; HRE: hexanucleotide (G4C2) repeat expansion; IDP: intrinsically disordered protein; ITC: isothermal titration calorimetry; LLPS: liquid-liquid phase separation; MD: molecular dynamics; MST: microscale thermophoresis; NHS: N-Hydroxysuccinimide, NPM1: Nucleophosmin; PBS: phosphate-buffered saline; PEG: polyethylene glycol; PSS: polystyrene sulfonate; PSS_Rhod: Rhodamine-labelled heterogenous mixture of PSS; RAN: repeat-associated non-AUG translation; Rg: radius of gyration; R-DPR: arginine-rich DPR; RDF: radial distribution function; RRM: RNA-recognition motif; sALS: sporadic amyotrophic lateral sclerosis; SCA36: spinocerebellar ataxia type 36; SG: stress granule; SV2: vesicle 2 protein; TDP-43: TAR DNA-binding protein 43; TEMED: N,N,N′,N′-tetramethyl ethylenediamine; ThS: thioflavin S; ThT: thioflavin T; XDP: X-linked dystonia Parkinsonism

Acknowledgements

This work was supported by an EC H2020-WIDESPREAD-2020-5 Twinning grant (PhasAge, no. 952334) and EC H2020-MSCA-RISE Action grant (IDPfun, no. 778247, and grants K124670 and K131702 from the National Research, Development and Innovation Office (NKFIH), Hungary, and the National Science Centre, Poland (grant no. 2018/31/D/ST5/01866) (P.B.) and grant no 2021/43/B/ST8/01900 for A.B-S. The contribution of a VUB Strategic Research Program on Microfluidics (SRP51) at Vrije Universiteit Brussel (VUB, Brussels, Belgium, to MVN, DM and PT), an FWO PhD fellowship in strategic basic research (FWOSB77, to JA) is also acknowledged. TL is holder of a postdoctoral innovation mandate (grant no. HBC.2022.0194) by the Flanders Innovation & Entrepreneurship Agency (VLAIO). We also thank the computational resources and services used in this work that were provided by the VSC (Flemish Supercomputer Center), funded by the Research Foundation - Flanders (FWO) and the Flemish Government, and Poland's high-performance computing infrastructure PLGrid (HPC Centers: ACK Cyfronet AGH) within computational grant no. PLG/2023/016229. The authors are indebted to Rani Baes (Microbiology, DBIT, VUB) for the RNA constructs provided for the EMSA experiments.

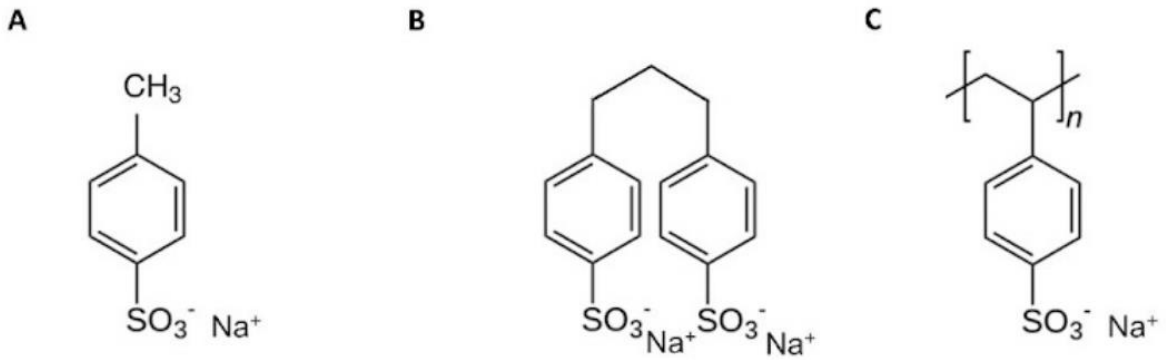

Scheme 1. *Chemical formula of polystyrene sulfonate (PSS) variants*

In this study, variants of polystyrene sulfonate (poly(sodium 4-styrenesulfonate), PSS) of different polymer length were used, such as A, n = 1 (monomer), B, n = 2 (dimer), and longer variants (C), i.e., n = 5 (pentamer), n = 22 (PSS_22) n = 43 (PSS_43), n* = 73 (PSS_Rhod, a heterogenous mixture of average Mw = 15 000 g/mol, fluorescently labelled with Rhodamine), n = 87 (PSS_87) and n = 340 (PSS_340).

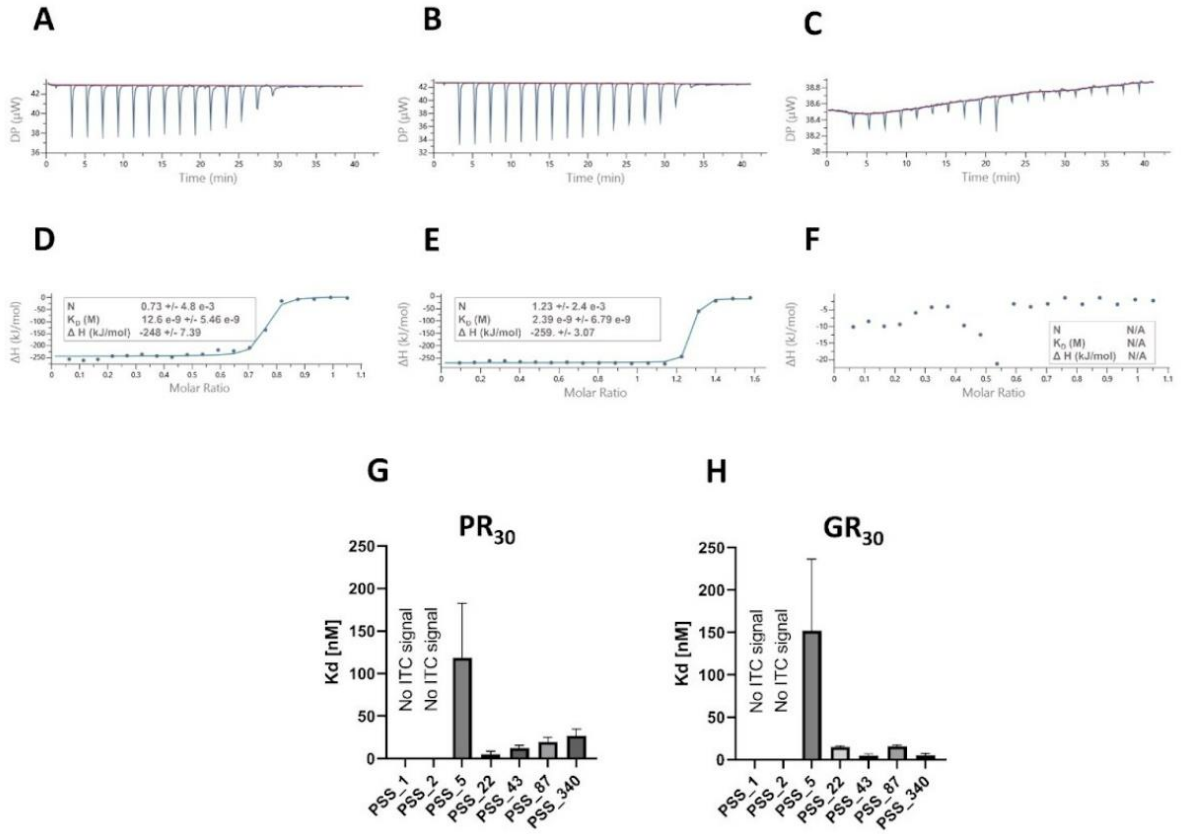

Figure 1. *Tight binding of DPRs by PSS*

The binding of PSS to DPRs (PR30, GR30 and PA30) was demonstrated and quantified by isothermal titration calorimetry (ITC). Three DPRs were titrated by different length variants of PSS. (A-C) raw ITC data with PSS_43, (D-F) integrated ITC data, with curves fit to the standard single binding site model. (G, H) As PA30 shows no signs of interaction, Kd is determined for PR30, and GR30 with all PSS variants (cf. Scheme 1) in 150 mM NaCl, pH 7.4.

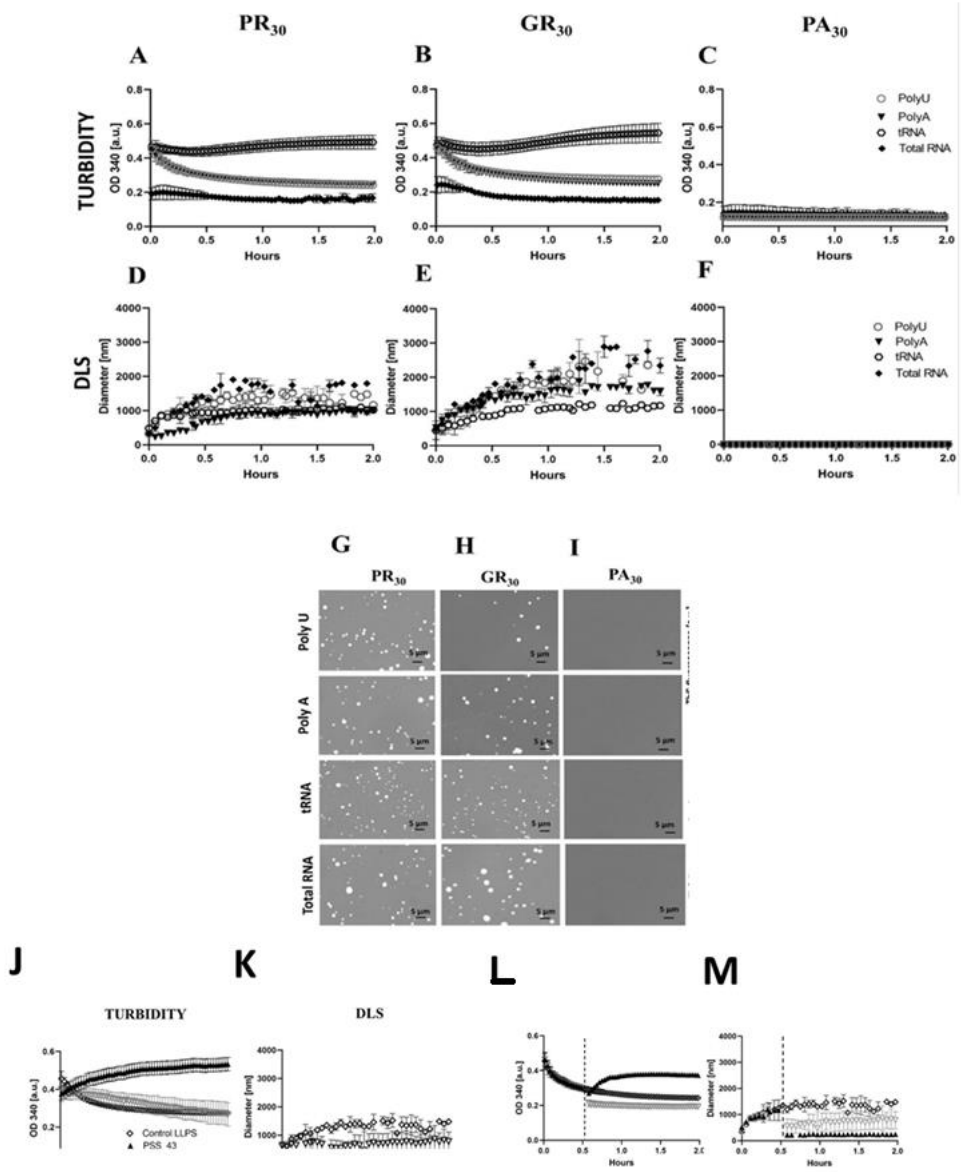

Figure 2 *Liquid-liquid phase separation of C9orf72 DPRs initiated by different RNAs.*

(A-F) LLPS of three different DPRs, PR30 (left column), GR30 (middle column) and PA30 (right column) was monitored by an increase in turbidity (OD340, A to C), and size of droplets by dynamic light scattering (DLS, D to F) in the presence of polyU, polyA, tRNA and total RNA extracted from Neuro-2a cells. Droplets were also visualized by fluorescence microscopy using DyLight 488-labelled DPRs mixed into 200x excess of unlabeled DPRs, following 15 min incubation (PR30 (G), GR30 (H), PA30 (I)). The experiments were performed in 10 mM HEPES, pH 7.4, 150 mM NaCl, at 50 µM DPR and 0.5 µg/µl RNA concentrations (K-N). LLPS of PR30 was then initiated by polyU in the presence of PSS_43 or the monomer of PSS, and monitored by adding PSS before (K, L) or 30 min after (M, N), initiating LLPS, by turbidity (OD340, on K, M) or DLS (on L, N). The experiments were performed at 150 mM NaCl, pH 7.4, at 50 µM PR30 and 0.5 µg/µl RNA concentration. The molar ratio of PSS_43 and the monomeric version was 1:43, which corresponds to the number of styrene sulfonate units in PSS_43.

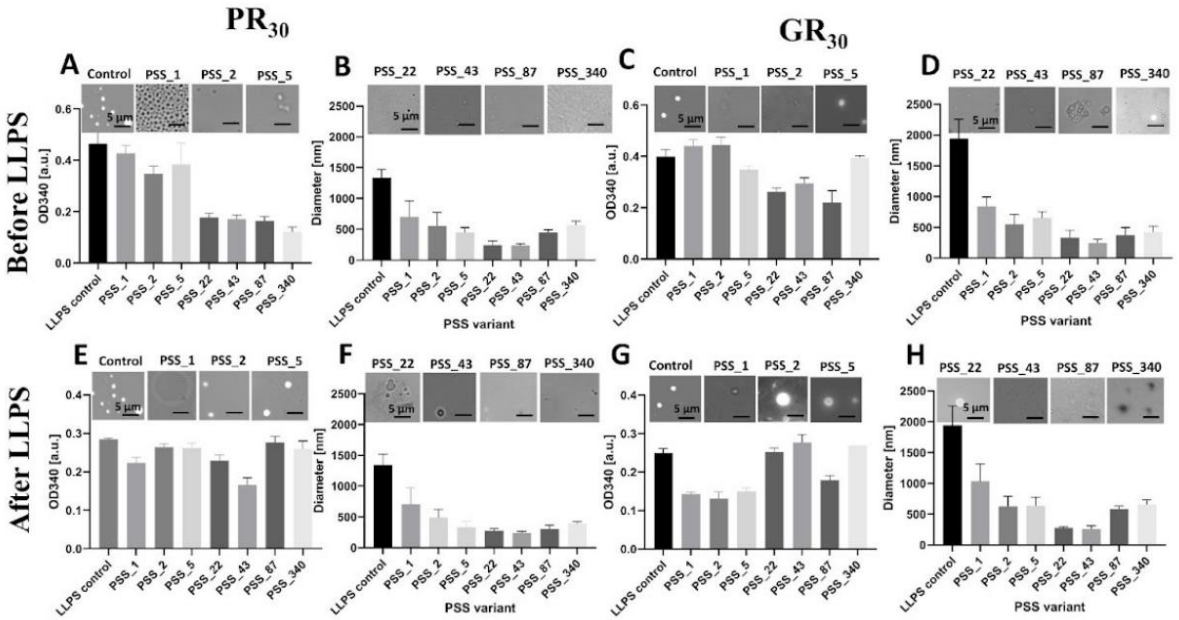

Figure 3. *Length-dependence of inhibition of the LLPS of R-DPRs by PSS*

LLPS of PR30 (A B, E, F) and GR30 (C, D, G, H) was initiated by polyU in the presence of different length variants of PSS, and monitored by turbidity (OD 340) and DLS, and visualized by microscopy (inserts), by adding PSS before (A-D) or 30 min after (E-H) initiating LLPS. The experiments were performed at 150 mM NaCl, pH 7.4, at 50 µM DPR and 0.5 µg/µl RNA concentration and at a PSS unit to DPR ratio 1:1.

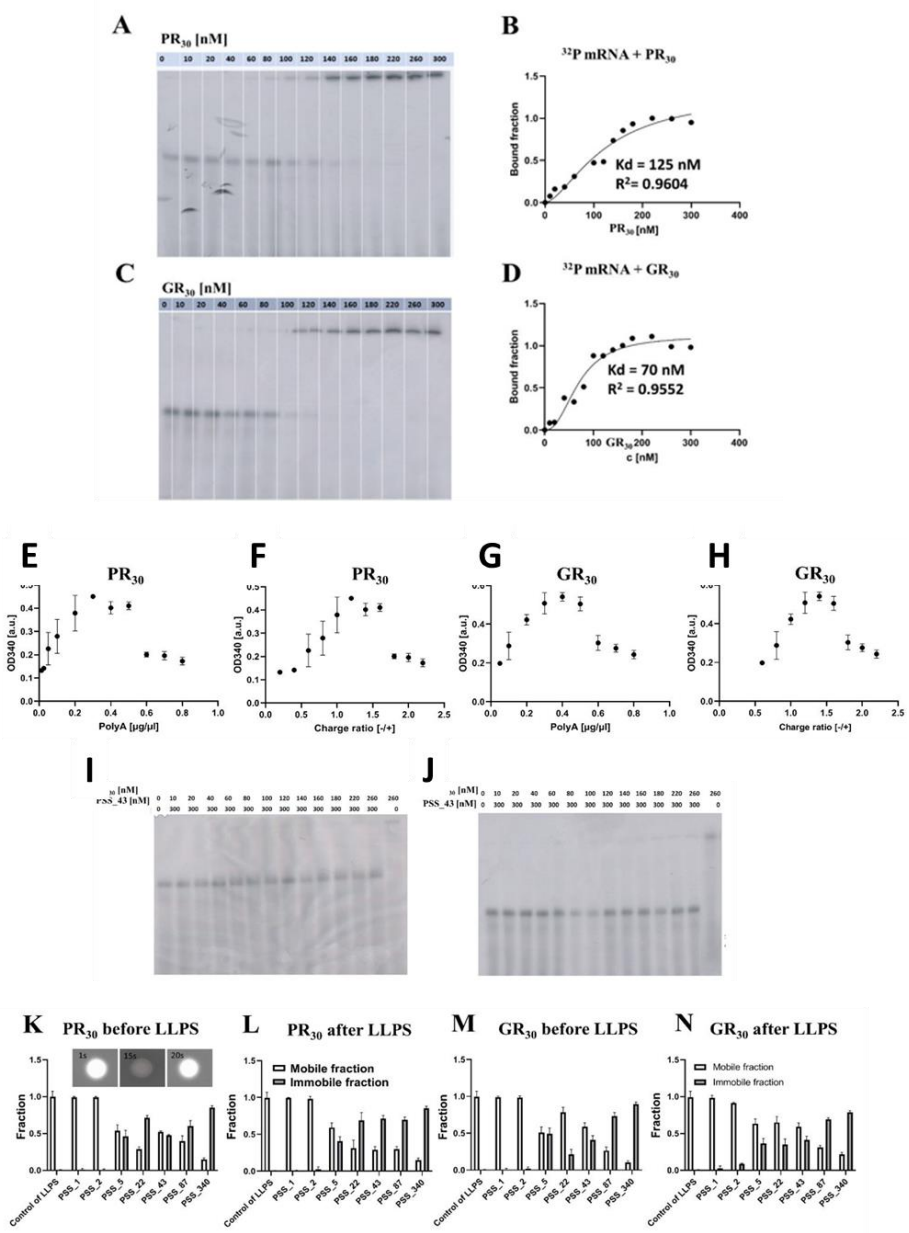

Figure 4. *Mechanism of LLPS and PSS effect on DPRs*

EMSA results show strong interactions between 32PmRNA and PR30 (A, B) and GR30 (C,D). The figures show the fraction of 32PmRNA band as PR30 (A, B) and GR30 (C, D) were titrated. The values for the Kd and Bmax obtained from the curve fitting are 125.4 +/- 1.2 nM and Bmax 1.307 +/- 0.05 for PR30 and 70.11 +/- 8.2 and Bmax 1.118 +/- 0.08 forGR30. RDPs titrated by polyA. The maximum of recorded turbidity (OD340) curves plotted as a function of polyA concentration (E, G) or RNA:R-DPR charge ratio (F, H) shows a maximum, i.e., reentrant behavior. Upon titrating 32PmRNA in the presence of an excess of PSS_43 (300 nM), the RNA always appears in the free (non-DPR complexed) state, except when no PSS is added (I, J). R-DPRs were treated with different variants of PSSs added before (K, M) or 30 min after (L, N) LLPS was initiated and % FRAP recovery (the fraction of fluorescence recovered, i.e., dynamic fraction of LLSP droplets), was determined; empty columns show fast recovering, whereas full columns show non-recovering, fraction of fluorescence.

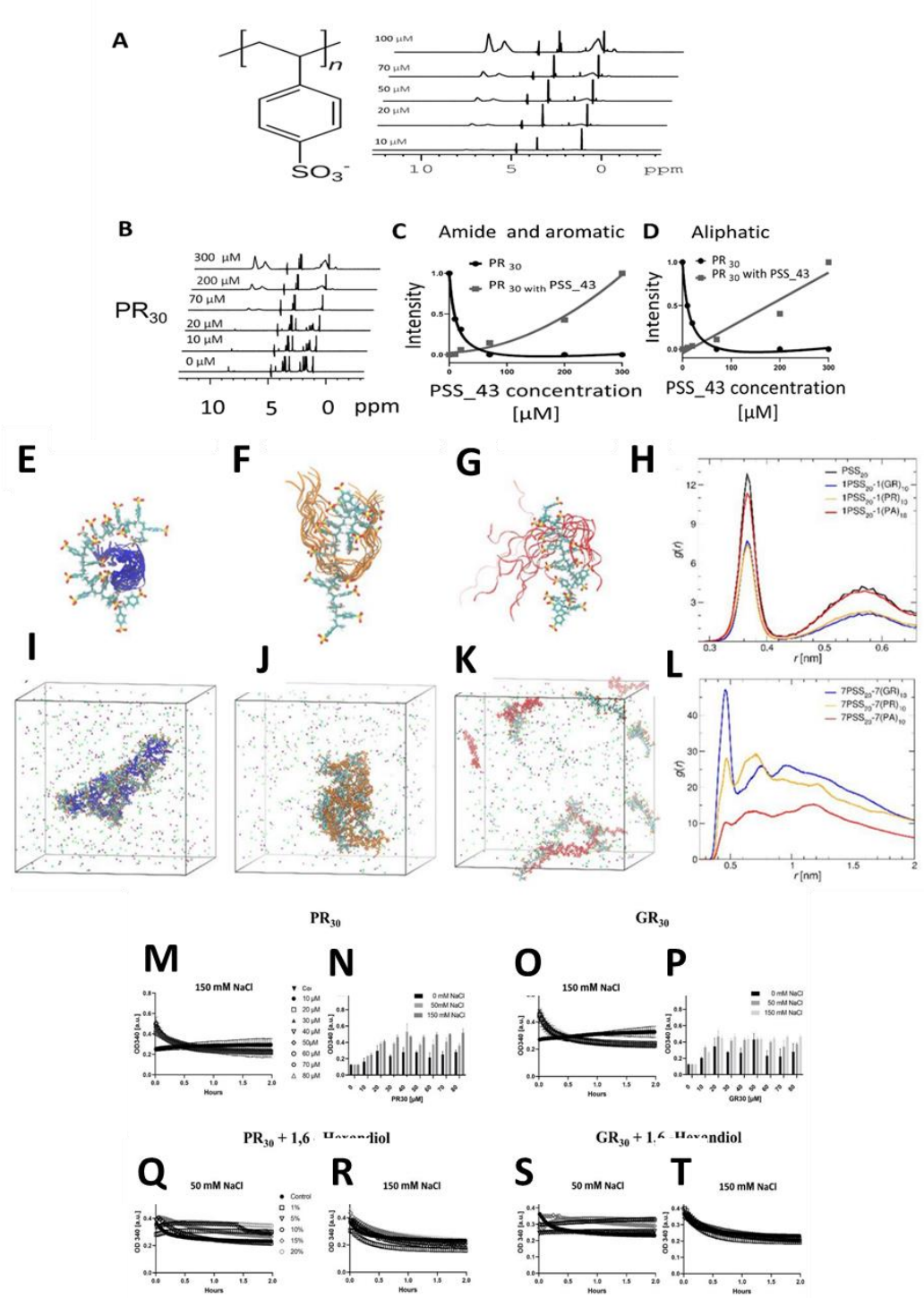

Figure 5. *Mechanism of PSS - R-DPR interaction*

$^{1}D^{1}H$ NMR Spectrum of PSS_43 (A) was recorded at different concentrations; peaks correspond to the chemical structure of PSS. The interaction of PSS with DPR PR30 (B - D) was followed by ^{1}D-^{1}H NMR: spectra of PR30 at 100 μM were recorded in the presence of increasing PSS_43 concentrations (B, up to 300 μM). Peak intensities in the aromatic and amide (6-9 ppm) and aliphatic (1-3 ppm) regions were integrated and plotted separately for the DPR and PSS as a function of PSS concentration (C, D).

MD simulation snapshots of 1 PSS_20 : 1 GR10 (E), 1 PSS_20 : 1 PR10 (F) and 1 PSS_20 : 1 PA10 (G) systems, aligned to the PSS_20 molecules. Peptide conformations, saved in 20 ns time intervals, are shown as ribbons. The radial distribution function (RDF) between the sulphur atoms of PSS and Na+ counterions in the mixtures and a single PSS_20 molecule as a reference, is shown (H). Snapshots after 300 ns of 7 PSS_20 : 7 GR10 (I), 7 PSS_20 : 7 PR10 (J) and 7 PSS_20: 7 PA10 (K) systems. The Na+ and Cl- ions are highlighted as green and pink spheres, respectively. The RDF between the Cα atoms of DPRs and the sulphur atoms of PSS are calculated (L); RDFs are averaged over three different initial configurations. All simulations were run at 150 mM NaCl concentration.

LLPS of PR30, and GR30 were monitored by turbidity (OD340) at different concentrations of DPRs (M-P), three ionic strength values (I = 0, 150, 500 mM) or five concentrations of hexanediol (Q-T). The concentration of DPR for the experiments with hexanediol was 50 µM, RNA in all experiments was added at 0.5 µg/µl.

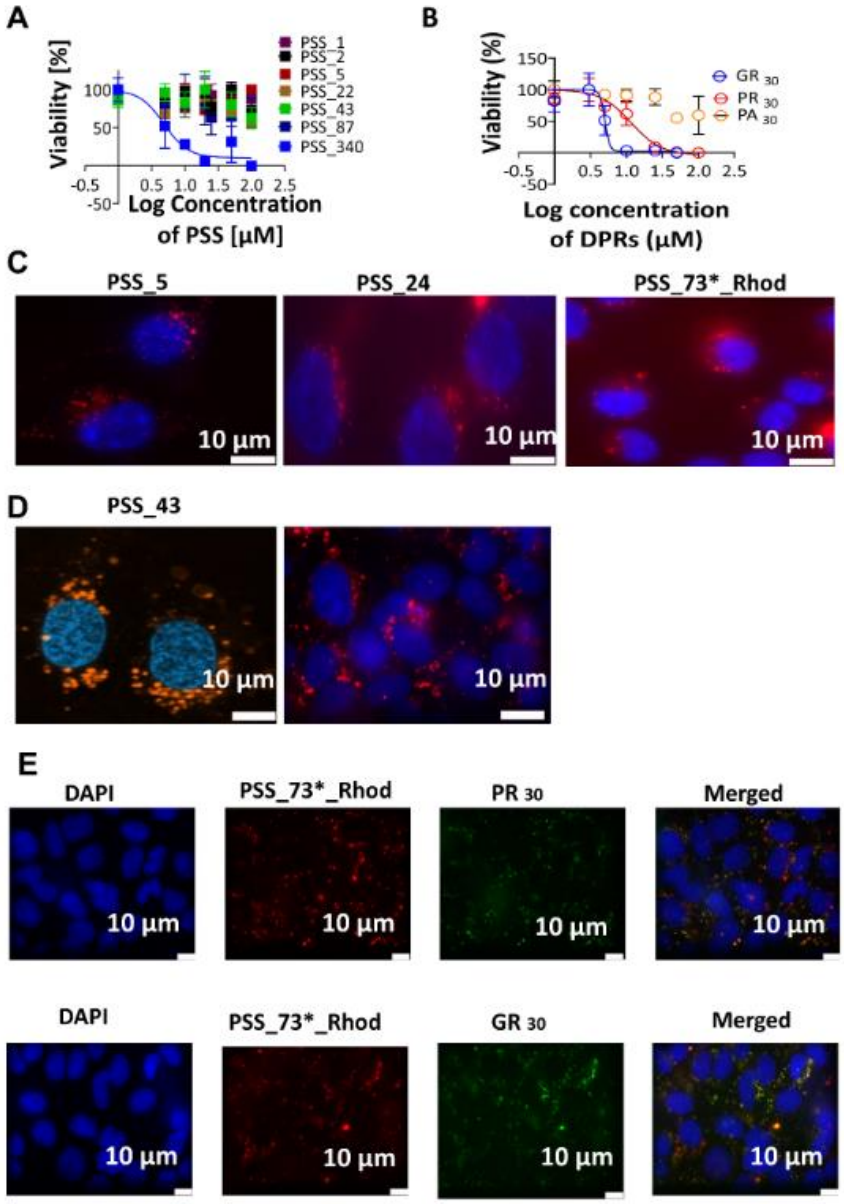

Figure 6. *PSS toxicity, cell penetration, and colocalization with R-DPRs*

Neuro 2a cells were treated with (A) different PSS length variants (from N = 1 to 340) and (B) different DPRs (PR30, GR30, and PA30) for 24h at concentrations up to 100 µM. Viability of cells following the treatment was assessed by total ATP content, yielding inhibitory concentrations (IC50): 5.3 ± 6.8 µM (PSS_340), 4.9 ± 2.4 µM (GR30), 12.8 ± 7.7 µM (PR30) and >30 µM (PA30). Shorter PSS variants appeared non-toxic under the given conditions. Potential cell penetration of PSS was addressed with fluorescence microscopy by fluorescently labelled PSS_73*_Rhod (a heterogeneous mixture), PSS_5_Rhod and PSS_22_Rhod in Neuro 2a cells (C) cells and PSS_73*_Rhod and PSS_43_Rhod in U2OS cells (D), at 10 µM concentration (or 0.12 µg/ml for PSS_73*_Rhod). Images were taken after 24 hr incubation. Colocalization of PSS with DPRs (E) was assessed by incubation of U20S cells with 0.12 µg/ml PSS_73*_Rhod for 2 h followed by 5 µM or 2 µM DyLight 488 NHS-labelled PR30 or GR30, respectively. Images were obtained after 24hr incubation. Cells were also labelled with 4,6-diamidino2-phenylindole (DAPI) for double-stranded DNA.

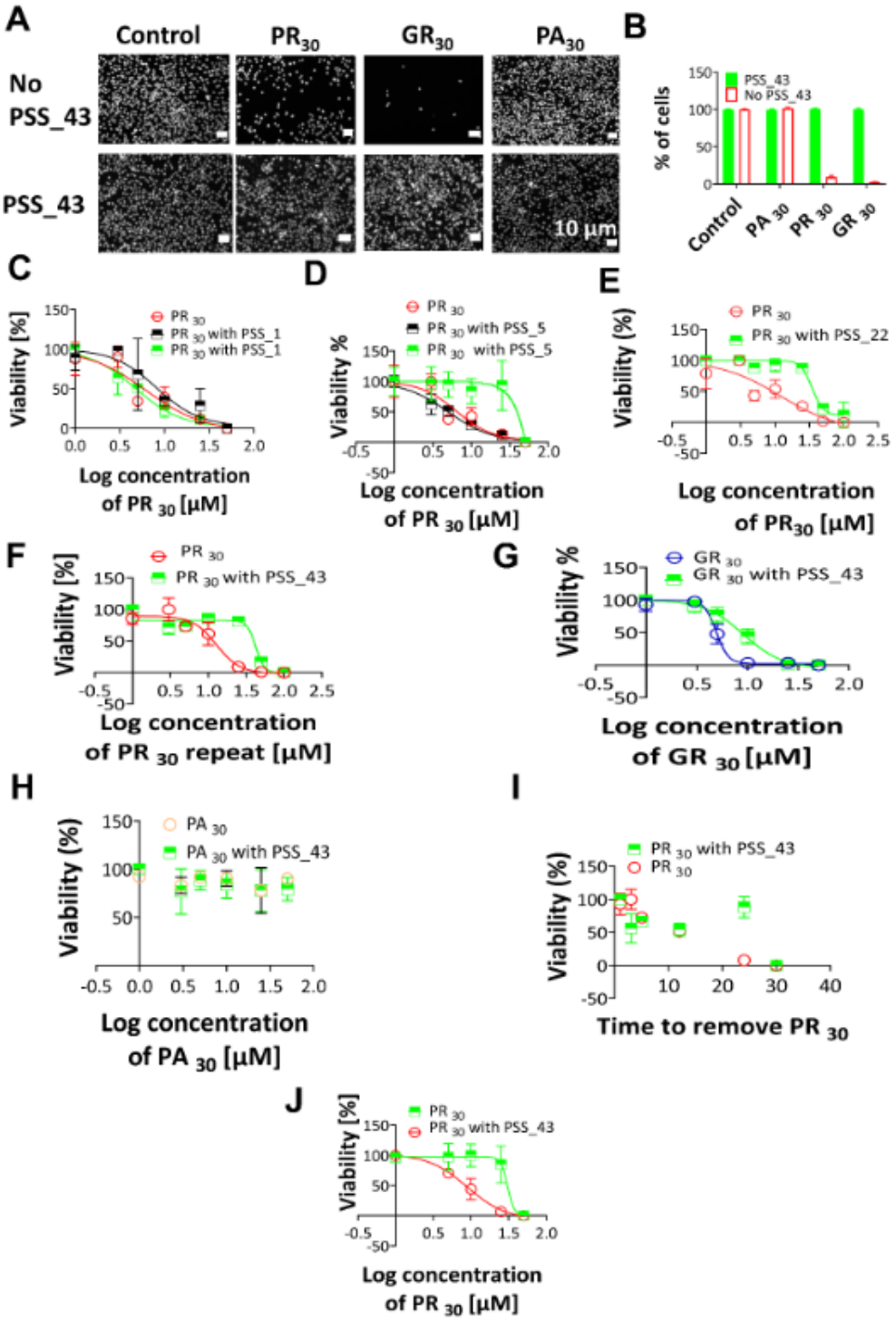

Figure 7. *Protection of cells by PSS against R-DPR toxicity*

Neuro 2a cells were first incubated without (control) or with three DPRs at 10 µM, in the absence or presence of 10 µM PSS_43. Microscopic images were recorded after 24 h incubation (A), from which total cell counts were determined (B). The protective effect of PSS against the toxicity of both PR30 and GR30 was also measured by adding the DPR at the indicated concentration together with PSS_1, PSS_5, PSS_22, PSS_43 at 20 µM and 200

μM, and ATP content of cells was measured after 24 h incubation (C, D, E, F, respectively). In a similar experiment (G), PSS_43 at 20 μM concentration was also incubated with GR30 at the concentration indicated and ATP content was measured after 24 h. (H) A similar experiment was also performed with PA30). The protective effect of PSS_43 was also measured by pre-incubating cells with 10 μM PR30 for the time indicated, removing it in a washing step and adding 10 μM PSS_43. Total ATP content was then measured after further 48h of incubation (I). In an experiment of the reverse order, cells were preincubated with 20 μM PSS_43 for 2 h, then PR30 was added at different concentrations indicated, and the ATP content was measured after 24 h incubation (J).

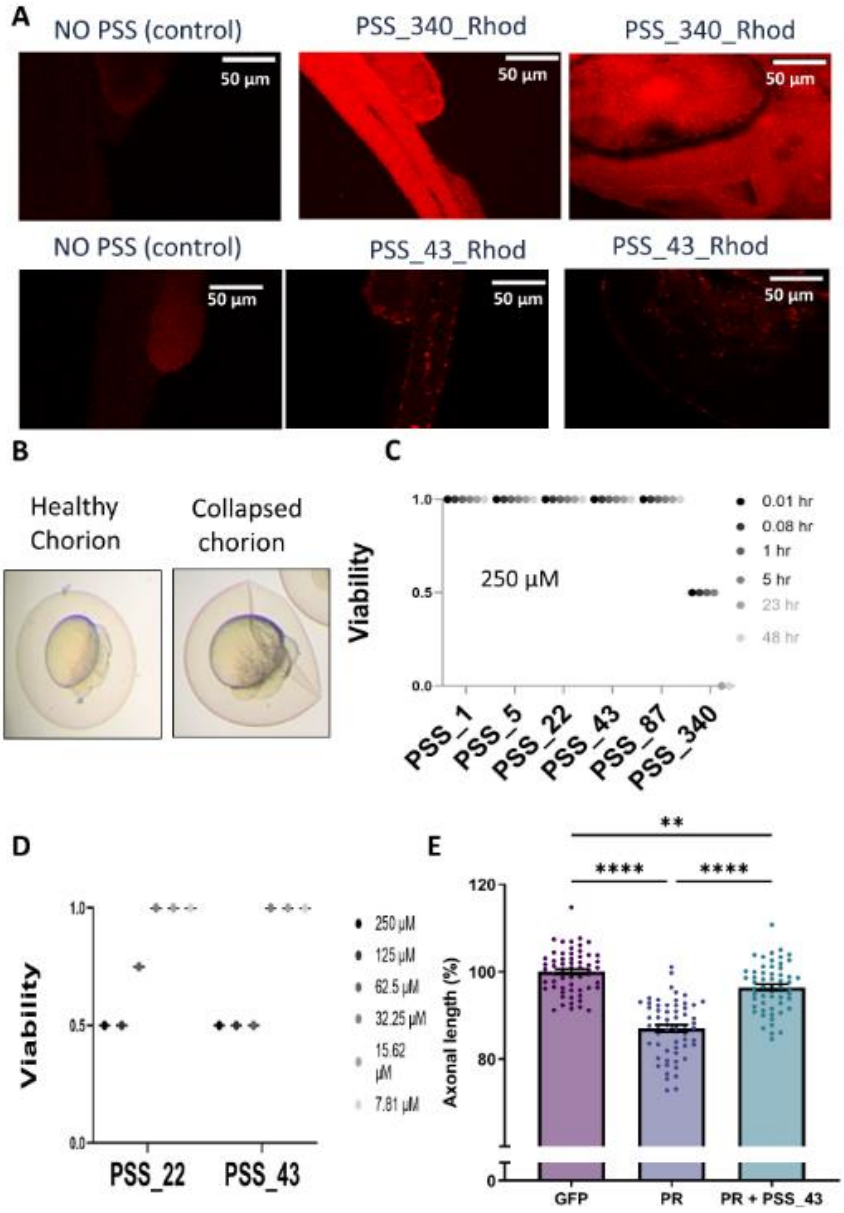

Figure 8. *Protection of Zebra embryos by PSS against R-DPR toxicity*

Zebrafish blastulas were manually dechorionated 6 h post-fertilization (hpf) and incubated with PSS_340 and PSS_43 for 24 h before imaging by confocal microscope (A). An embryo with healthy and collapsed chorion, as result of PSS toxicity, is shown (B). Embryos with chorion were incubated at 250 µM of different variants of PSS (PSS_1, PSS_5, PSS_ 22, PSS_43, PSS_87, PSS_340). They were visualized for up to 48 hr (C). Zebrafish blastulas were incubated with PSS_22 and PSS_43 at different concentrations up to 250 µM after dechorionated at 6 hpf and embryos were visualized at 30 hpf to observe survival (D). mRNA encoding for PR50 or GFP was injected at the 1-2 cell stage and Dechorionated 6 hpf and PSS_43 was added at 15 µM concentration. Embryos were fixed at 30 hpf and immunostained with anti-SV2 antibody to determine axon length (E).

Supplementary material

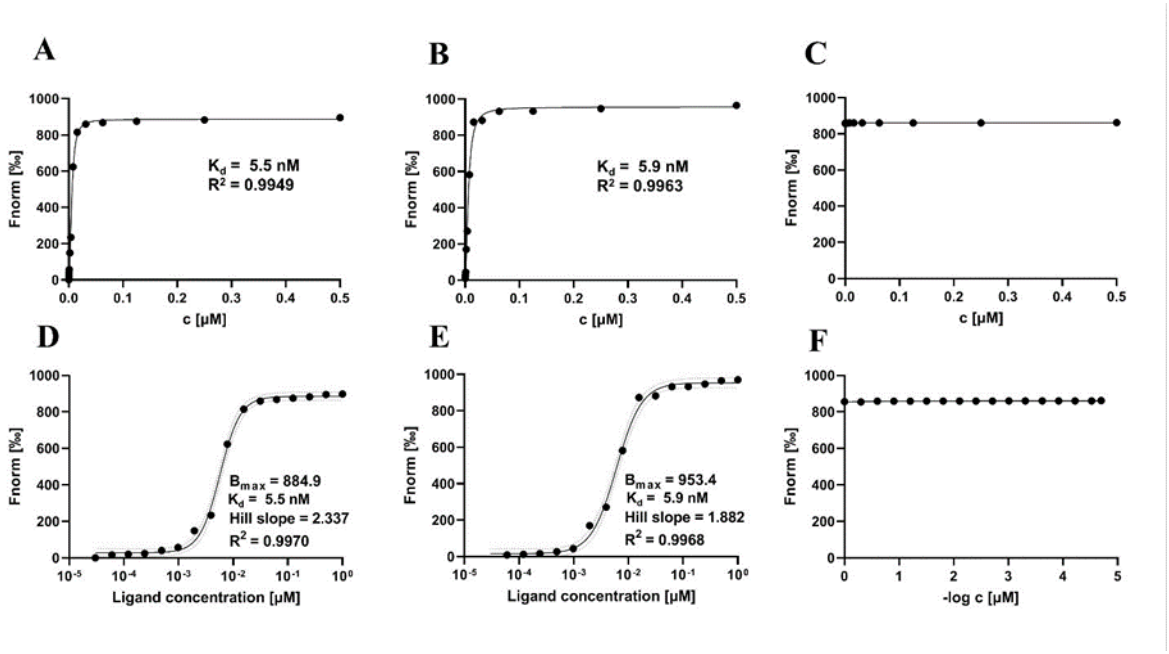

Suppl. Fig. S1. *Tight binding between DPRs and PSS_43*

Binding was measured by MST (L-R), the binding curves of PSS_43 and PR30 (L,O), GR30 (M,P), and PR30 (N,R) in a buffer of 10 mM HEPES, 150 mM NaCl, 0.05 % Tween are shown. The concentration of DPRs (labelled with Red-N-Hydroxysuccinimide (Red-NHS), 2nd generation dye from Nanotemper) was 2 µM, while concentration of PSS_43 varied from 0.03 nM to 500 nM. Measurements were repeated three times and data points are averaged with SEM, maximum fluorescence (Bmax) and R2. For all MST curves, apparent IC50 values were calculated using the Hill-equation.

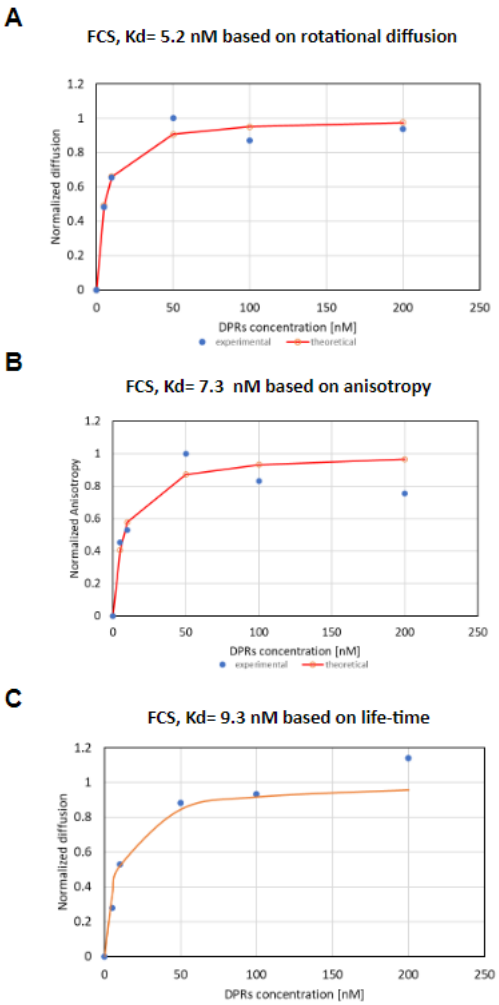

Suppl. Figure S2. Single-molecule fluorescence measurement of PSS_43 - PR30 binding

Kd of PSS-43 – PR30 binding was determined by single-molecule fluorescence, based on measuring rotational diffusion (A), anisotropy (B) and fluorescence life-time (C) of DyleLight 488-labeled PR30.

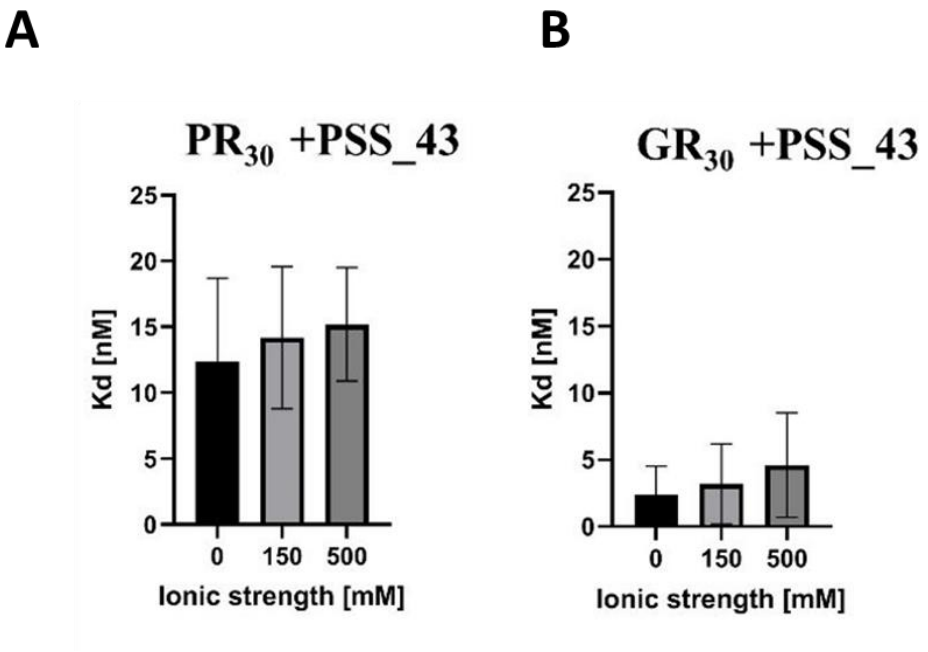

Suppl. Figure S3. *Salt titration of PSS - R-DPR systems*

PR30 and GR30 was titrated by PSS_43, and Kd of interaction measured by ITC, at various salt concentrations (0 mM, 150 mM and 500 mM).

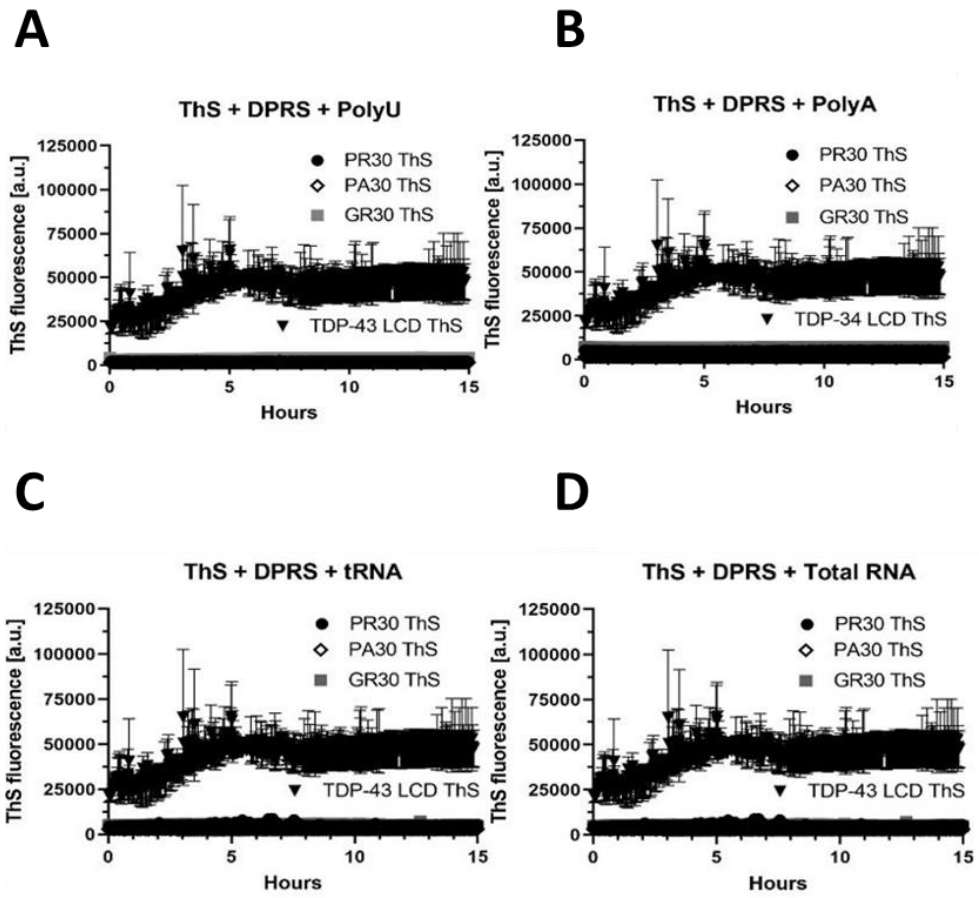

Suppl. Figure S4 *ThT and ThS curves of R-DPR - RNA systems*

LLSP of R-DPRs was initiated by the RNA indicated and followed over a time period of 15 h, in the presence of ThS, to indicate the possible transition to an aggregated state

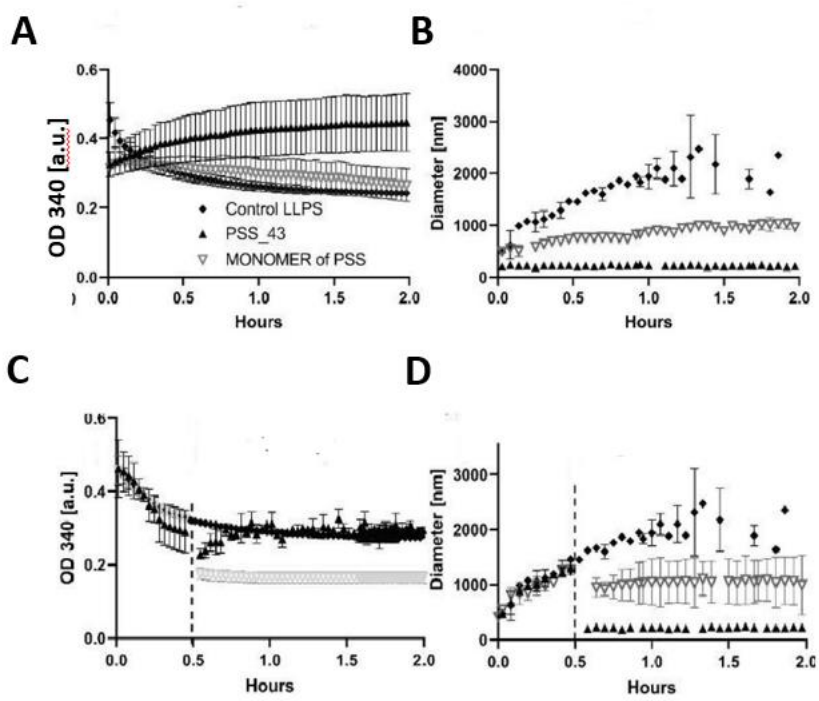

Suppl. Figure S5. *Effect of PSS_43 on GR30 LLPS*

LLPS of GR30 was initiated by polyU in the presence of PSS_43 or the monomer of PSS, and monitored by adding PSS before (A, B) or 30 min after (C, D) LLPS. The LLPS was followed by turbidity (OD340, A, C) or DLS (B, D). The experiments were performed at 150 mM NaCl, pH 7.4, at 50 µM PR30 and 0.5 µg/µl RNA concentration. The molar ratio of PSS_43 and the monomeric version was 1:43, which corresponds to the number of styrene sulfonate units in PSS_43.

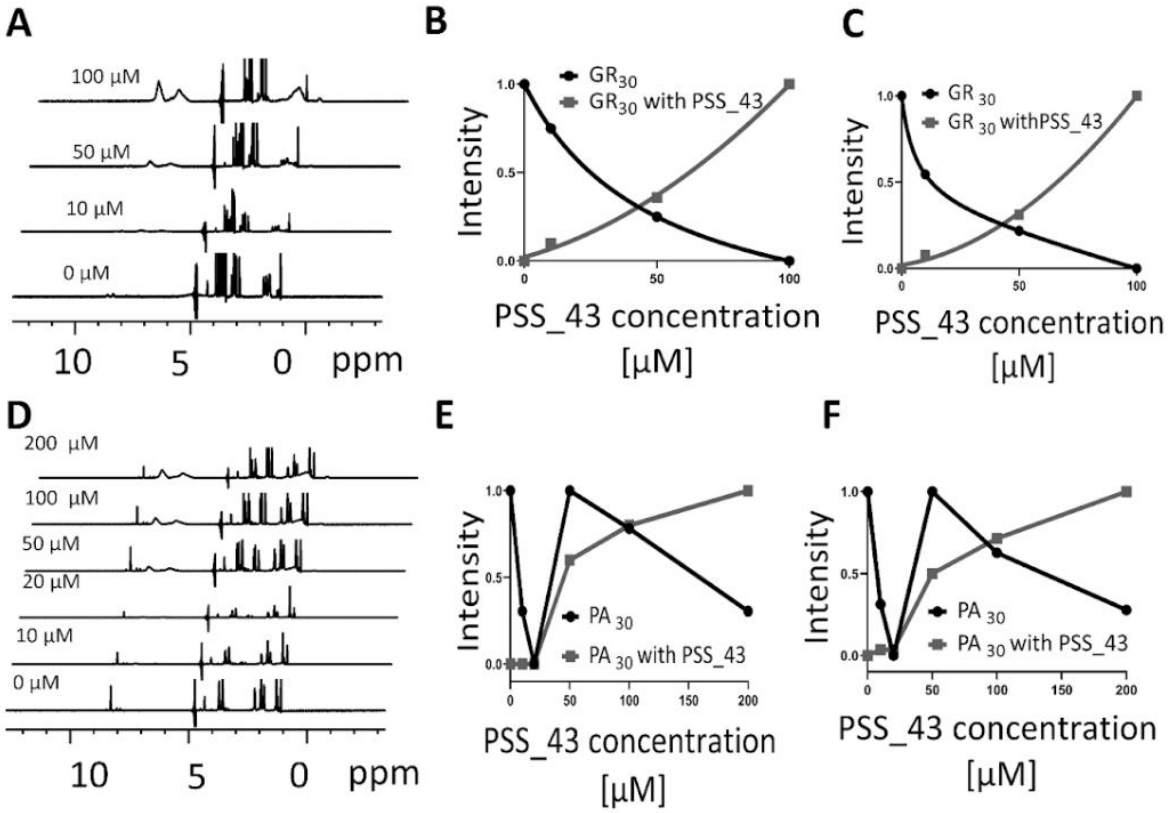

Suppl. Figure S6. *NMR of PSS - GR30 and PSS - PA30 systems*

$^{1}D^{1}H$ NMR spectrum of DPR PR30 (A) and PA30 (D) was recorded in the presence of increasing PSS_43 concentrations (up to 300 µM). Peak intensities in the aromatic and amide (6-9 ppm) and aliphatic (1-3 ppm) regions were integrated and plotted separately for the DPR and PSS as a function of PSS concentration for GR30 (B, C) and PA30 (E, F).

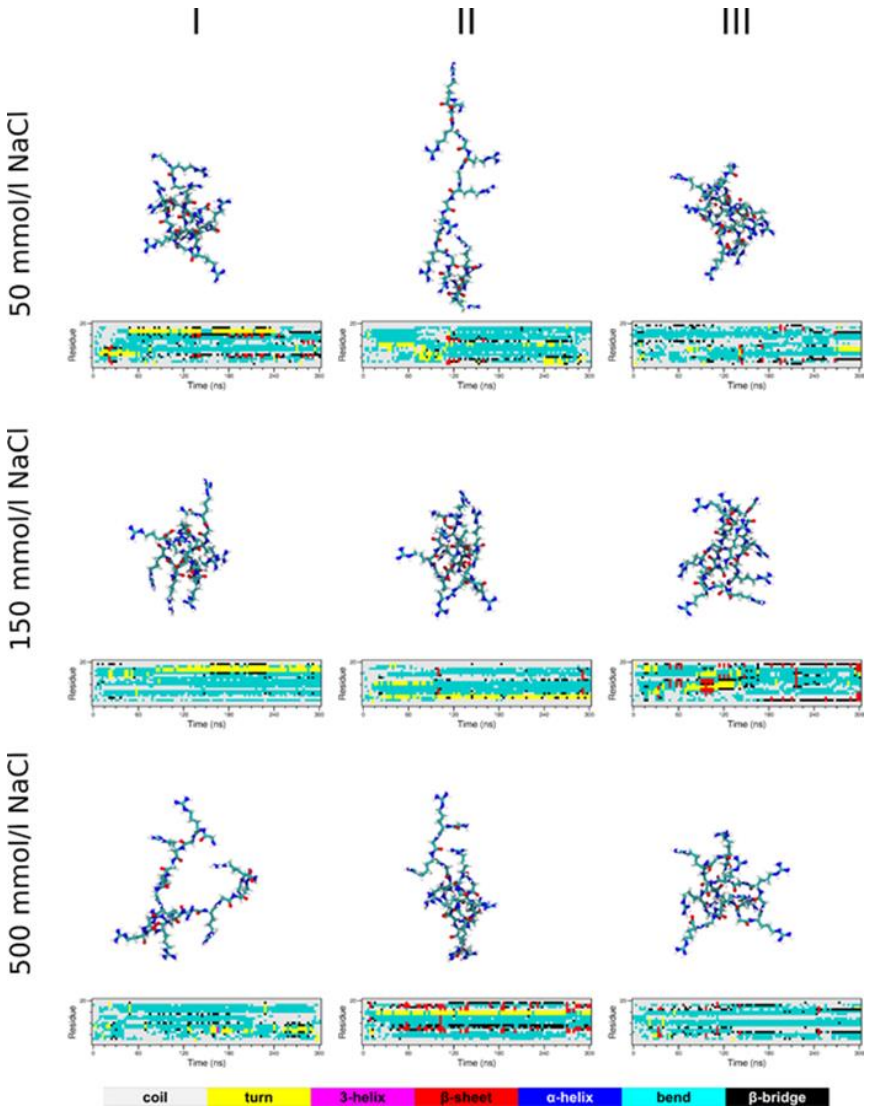

Suppl. Figure S7. *GR10 peptide conformations in MD simulations*

Representative conformations are shown after 300 ns MD simulations and its secondary structure evolution at various NaCl concentrations. Results for the three different initial configurations (I, II, and III) are presented in columns.

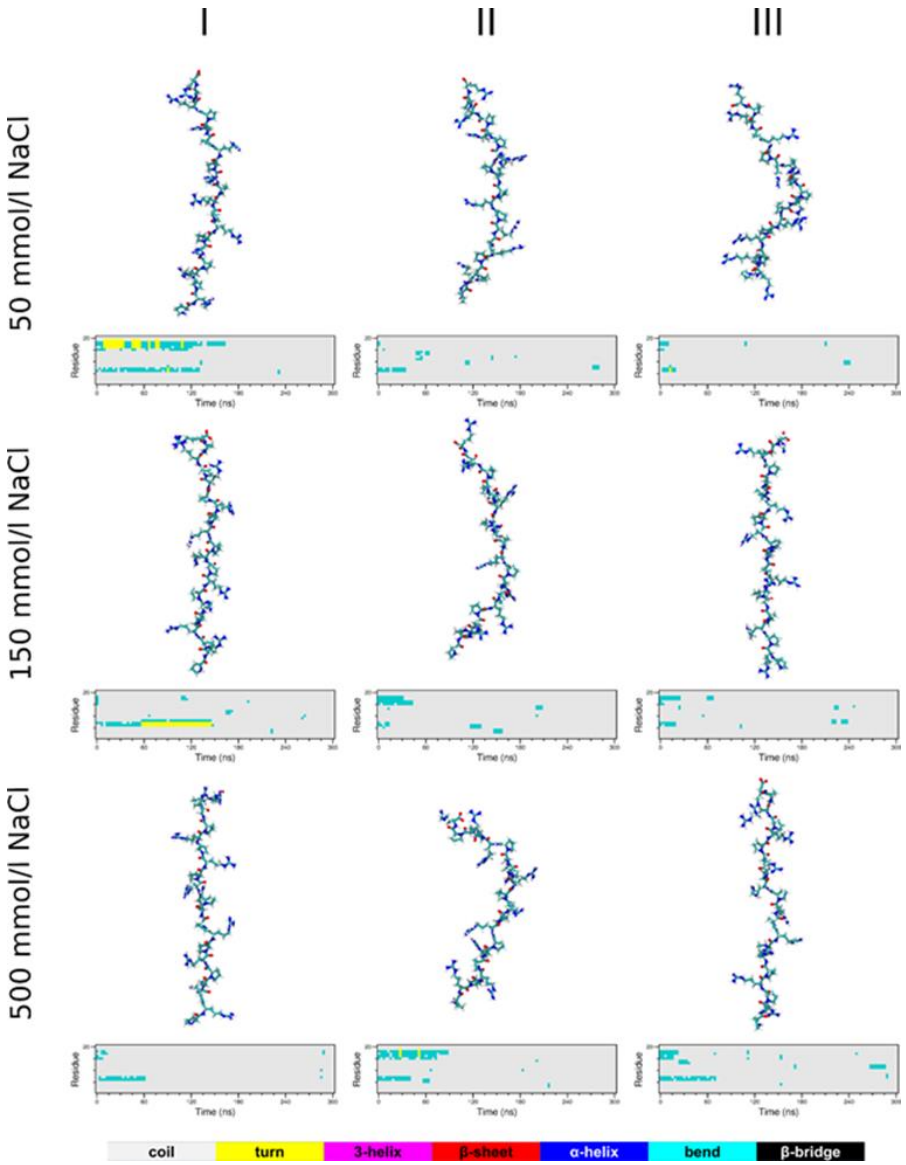

Suppl. Figure S8. *PR10 peptide conformations in MD simulation*

Representative conformations after 300 ns MD simulations and its secondary structure evolution at various NaCl concentrations. Results for the three different initial configurations (I, II, and III) are presented in columns.

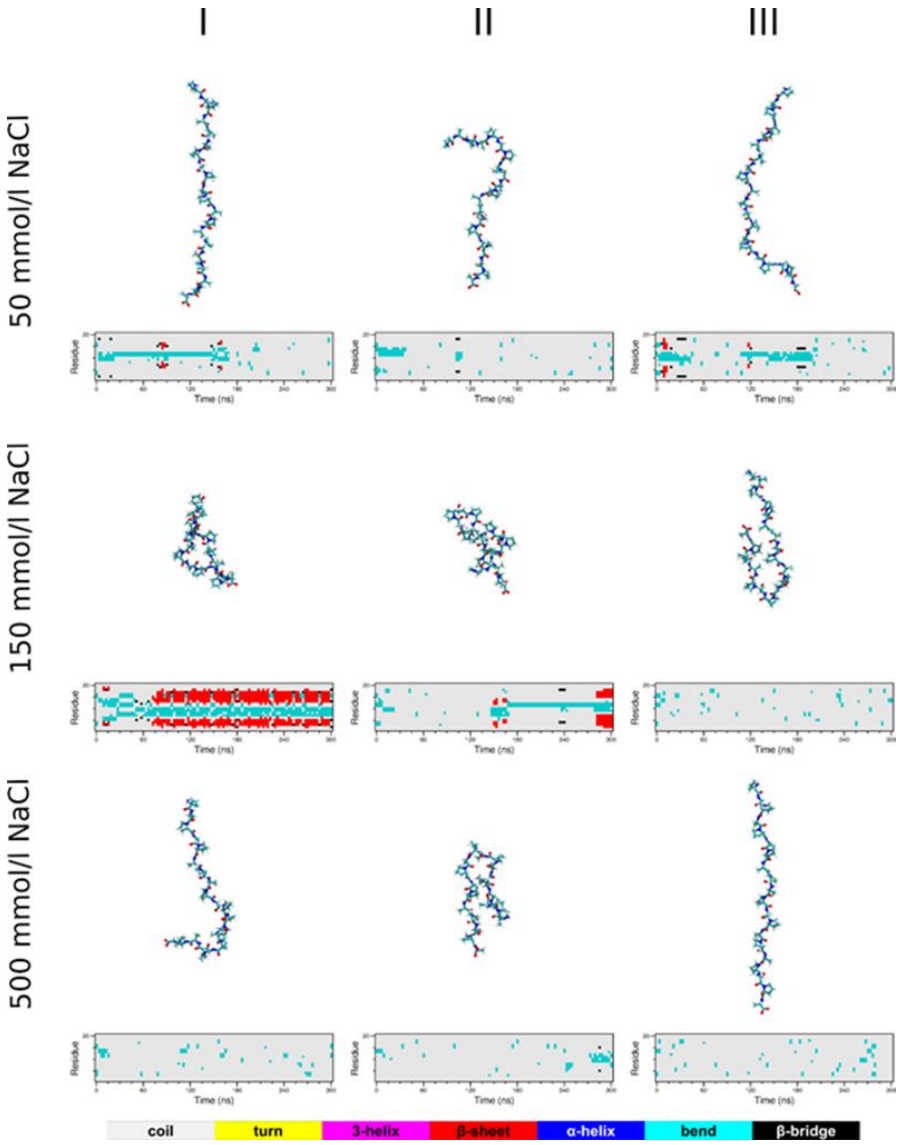

Suppl. Figure S9. *PA10 peptide conformations in MD simulations*

Representative conformations after 300 ns MD simulations and its secondary structure evolution at various NaCl concentrations. Results for the three different initial configurations (I, II, and III) are presented in columns.

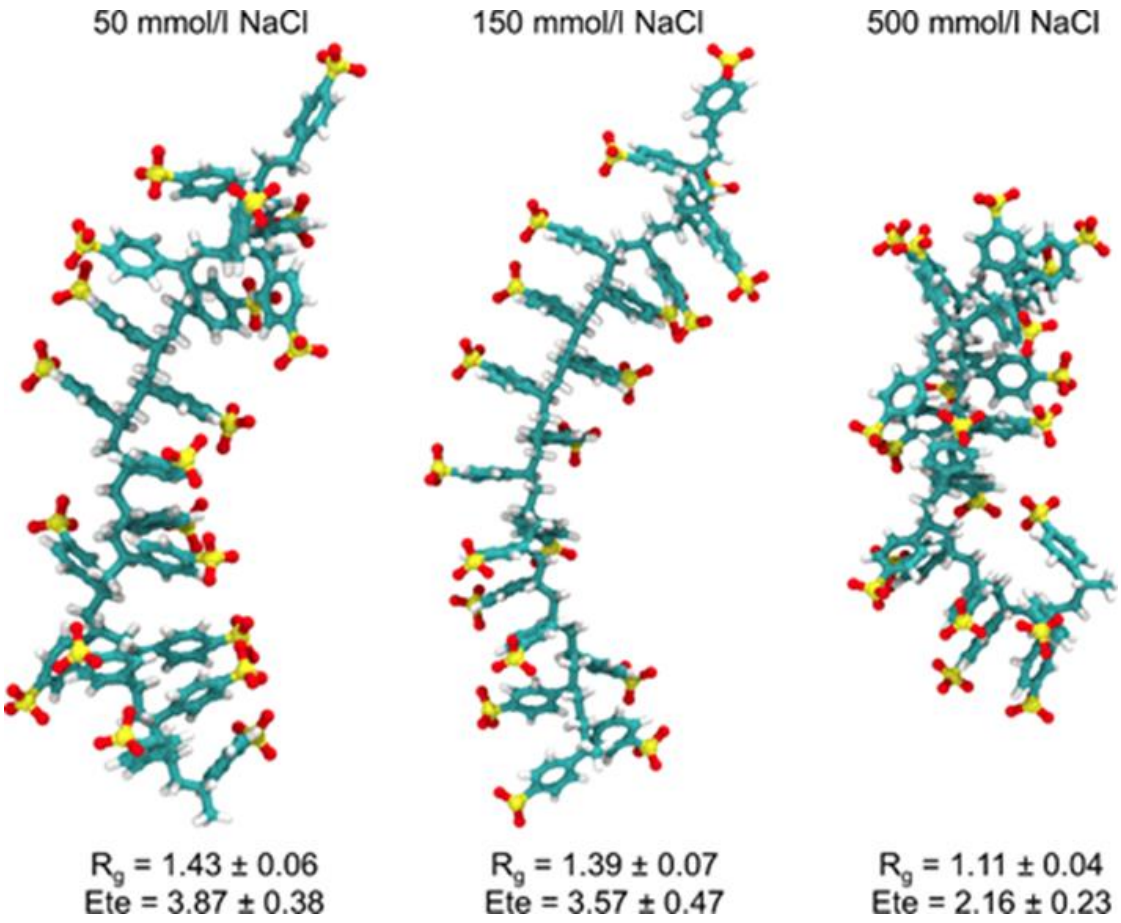

Suppl. Figure S10. *PSS20 conformations in MD simulation*

Representative conformations after 100 ns MD simulations at various NaCl concentrations, along with their radius of gyrations (Rg) and end-to-end distances (Ete), averaged over the last 50 ns.

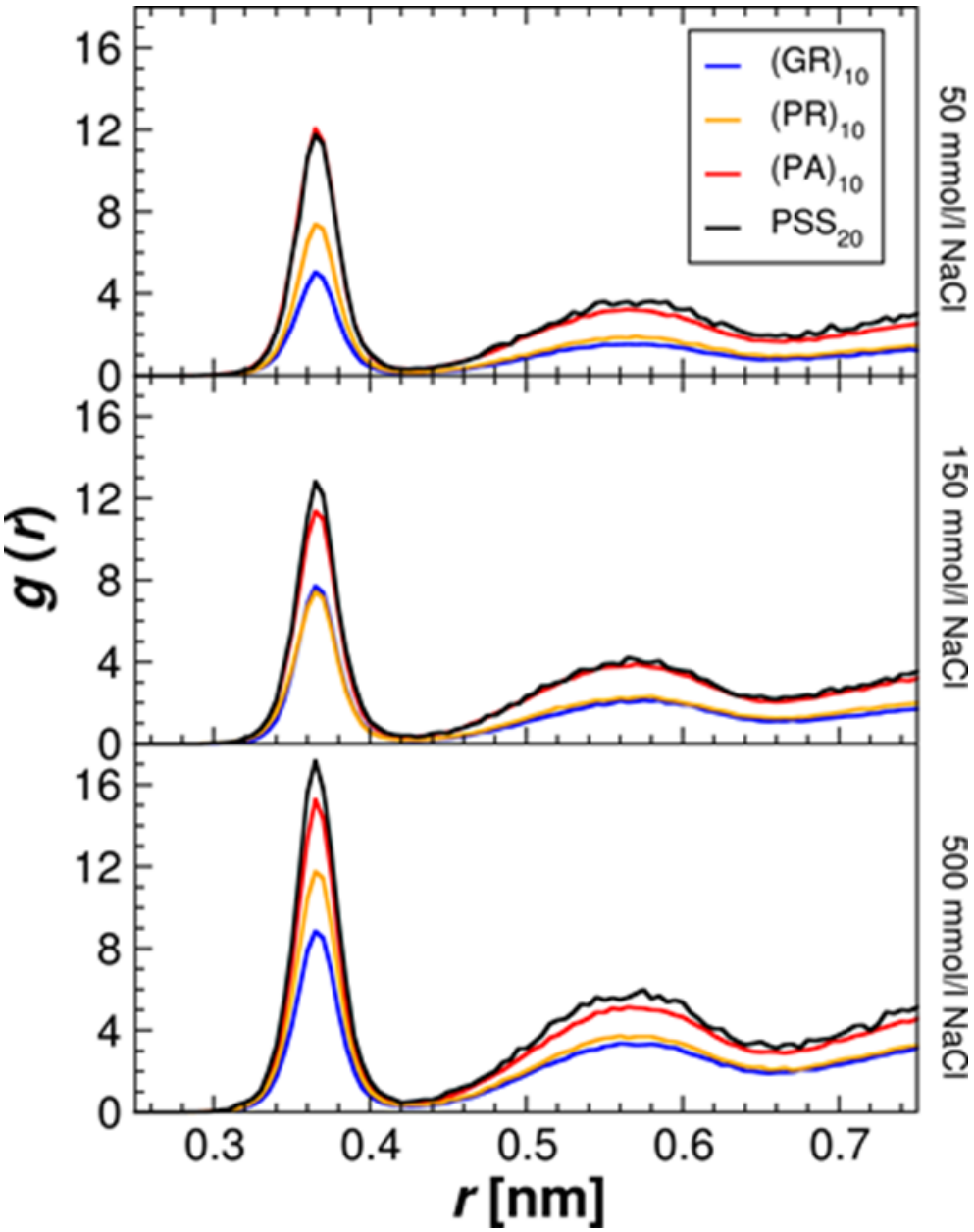

Suppl. Figure S11. *The radial distribution function (RDF) of trajectories of MD simulations*

MD simulations of GR10, PR10, P!10 and PSS_20 were analyzed for RDF, as defined between the S atom from PSS and Na+ counterion in the investigated 1:1 PSS20-Peptide systems at various NaCl concentrations.

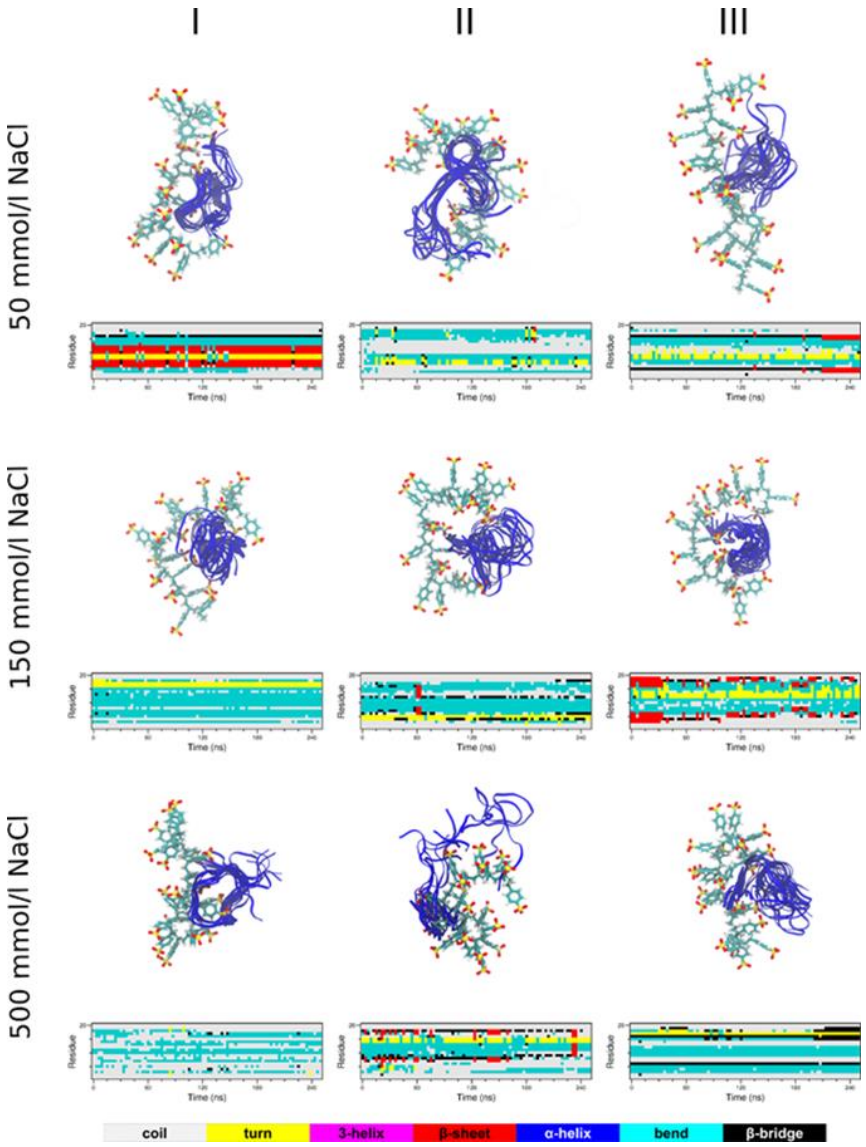

Suppl. Figure S12. *MD simulation snapshots of GR10-PSS20 systems*

Representative conformations are shown of trajectories at various NaCl concentrations, aligned to the PSS20 molecule. GR10 conformations, saved every 20 ns, are shown as blue ribbons. The secondary structure evolution of GR10 is shown below the snapshots. Results for the three different initial configurations (I, II, and III) are presented in columns.

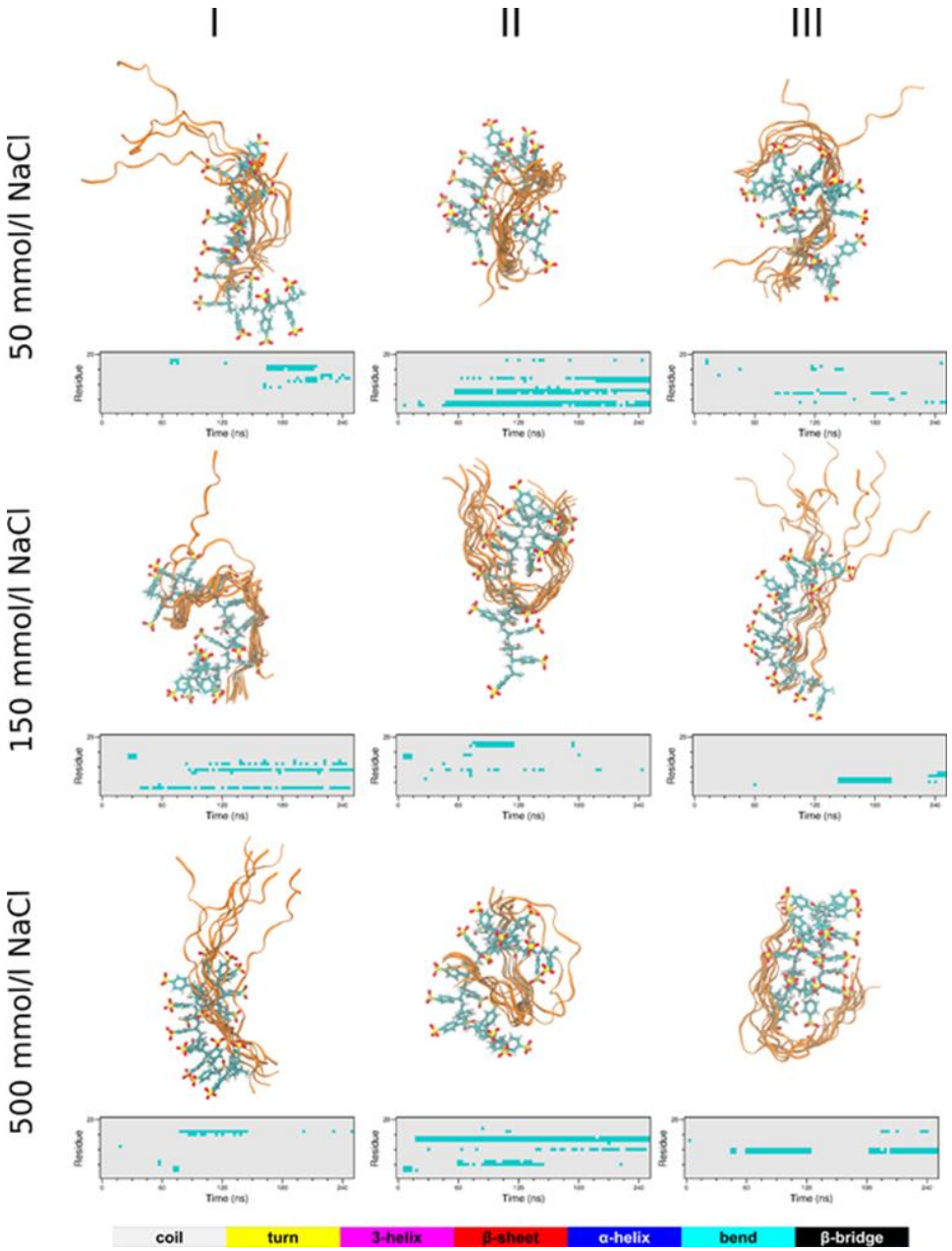

Suppl. Figure S13. *MD simulation snapshots of PR10-PSS20 systems*

Representative conformations are shown of trajectories at various NaCl concentrations, aligned to the PSS20 molecule. PR10 conformations, saved every 20 ns, are shown as orange ribbons. The secondary structure evolution of PR10 is shown below the snapshots. Results for the three different initial configurations (I, II, and III) are presented in columns.

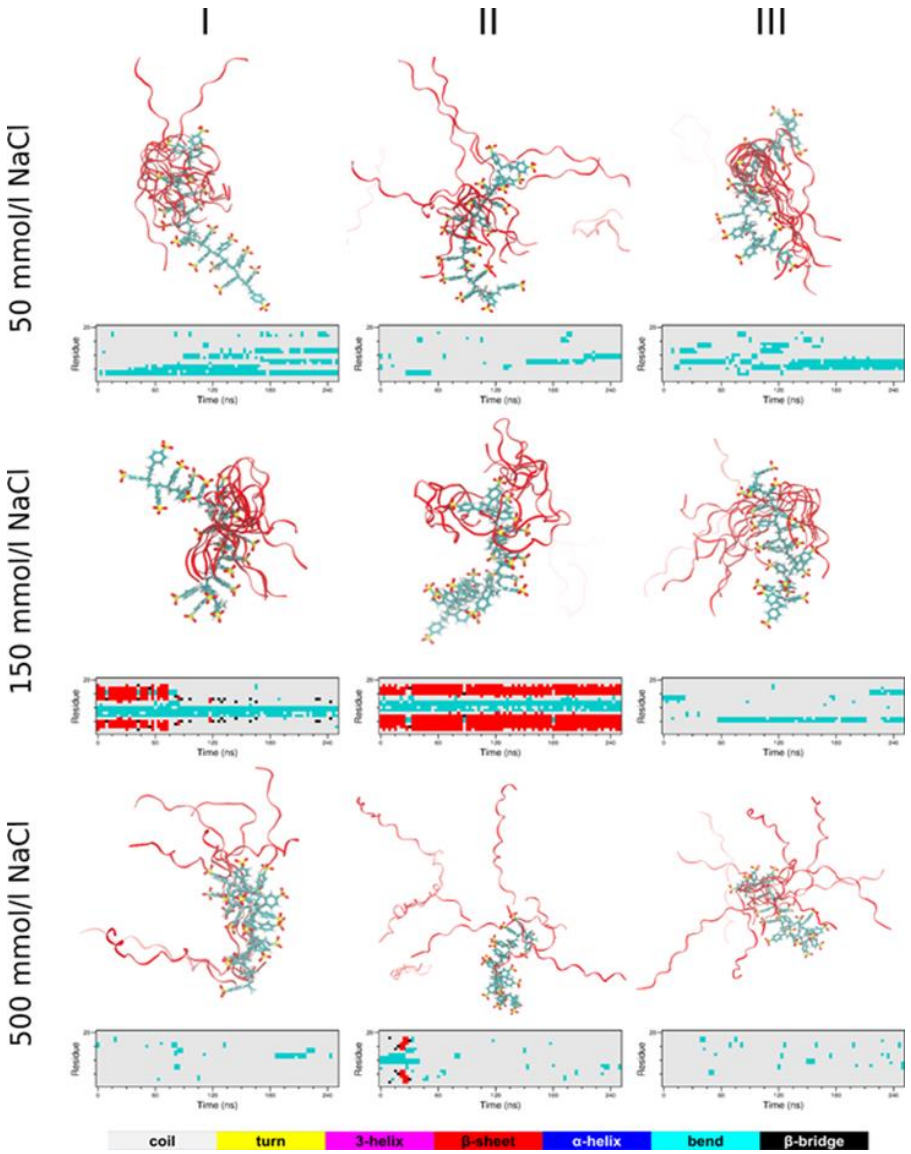

Suppl. Figure S14. *MD simulation snapshots of PA10-PSS20 systems*

Representative conformations are shown of trajectories at various NaCl concentrations, aligned to the PSS20 molecule. PA10 conformations, saved every 20 ns, are shown as red ribbons. The secondary structure evolution of PA10 is shown below the snapshots. Results for the three different initial configurations (I, II, and III) are presented in columns.

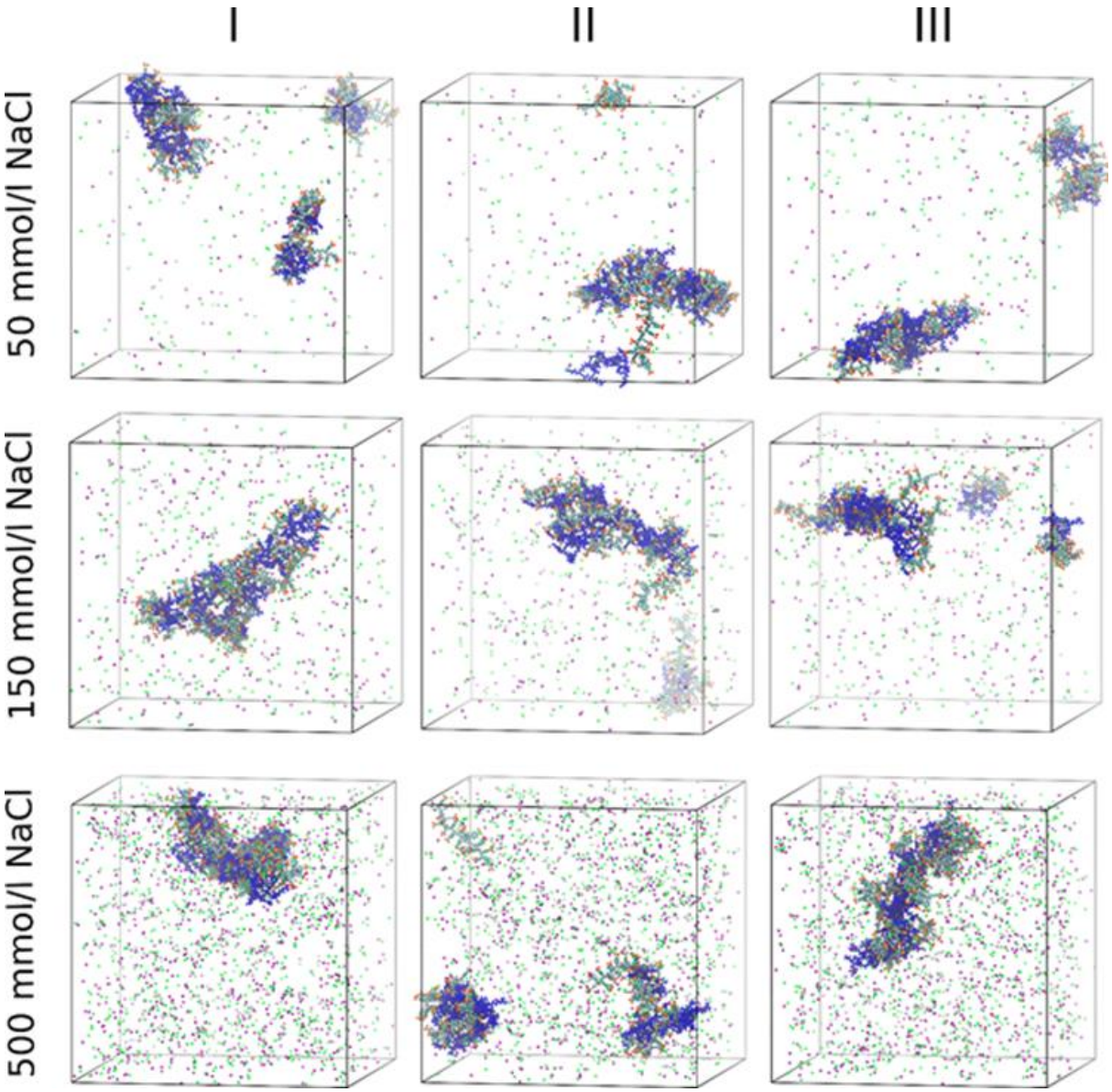

Suppl. Figure S15. *MD simulation snapshots of 7PSS20-7GR10 systems*

Representative conformations are shown of trajectories at various NaCl concentrations. GR10 molecules are highlighted in blue. The Na+ and Cl- ions are highlighted as green and pink spheres, respectively. Results for the three different initial configurations (I, II, and III) are presented in columns.

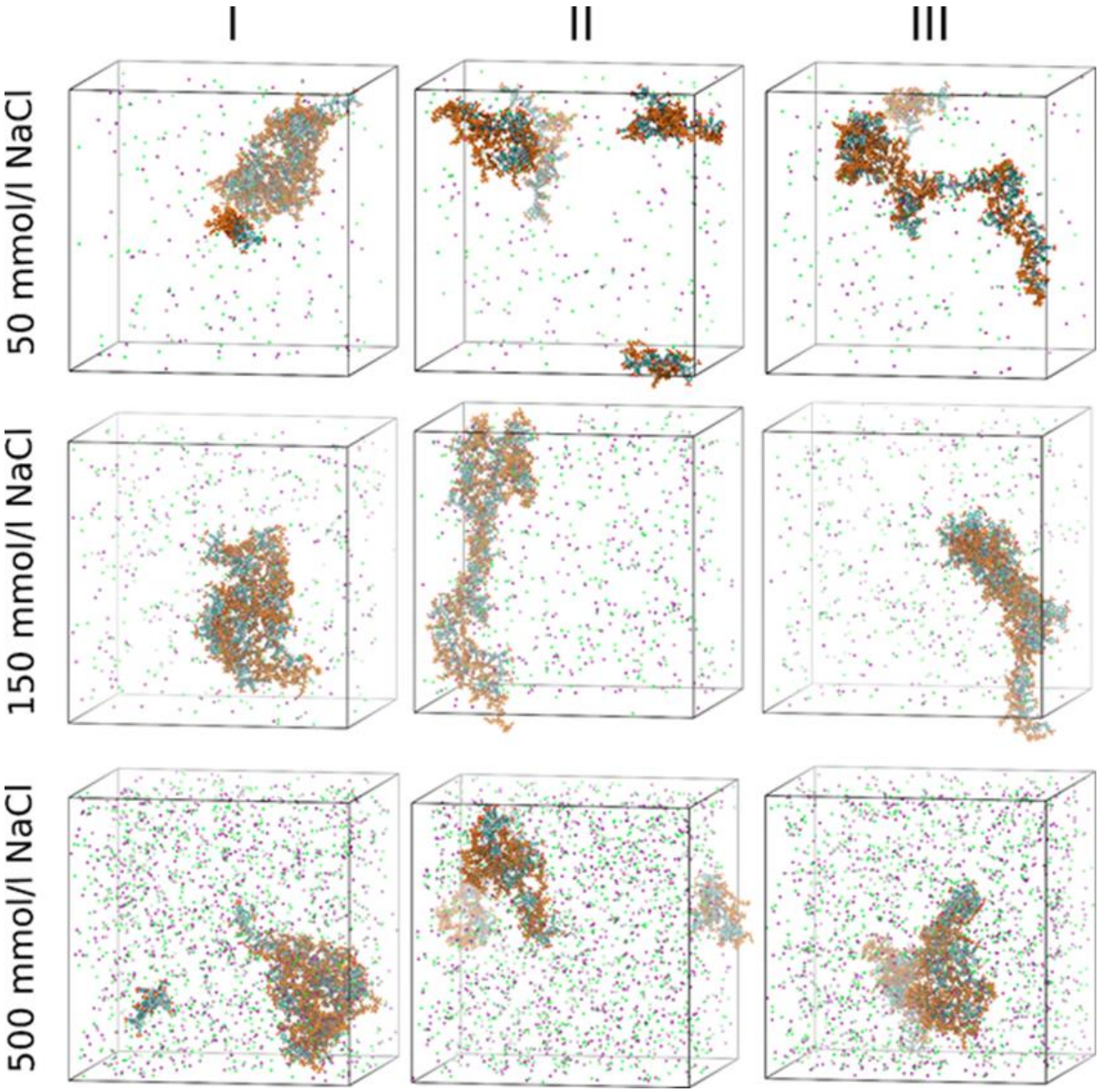

Suppl. Figure S16. *MD simulation snapshots of 7PSS20-7PR10 systems*

Representative conformations are shown of trajectories at various NaCl concentrations. PR10 molecules are highlighted in orange. The Na+ and Cl- ions are highlighted as green and pink spheres, respectively. Results for the three different initial configurations (I, II, and III) are presented in columns.

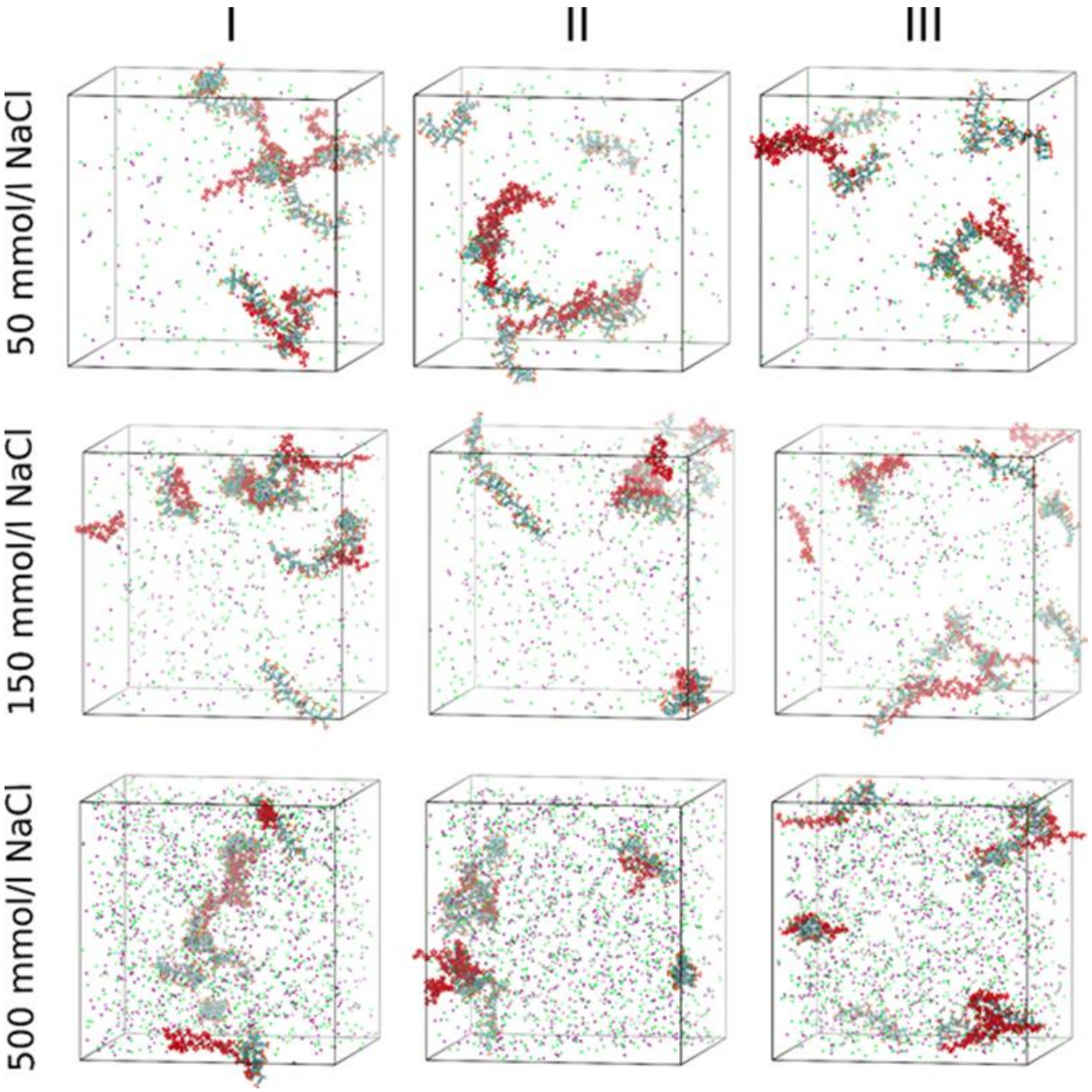

Suppl. Figure S17. *MD simulation snapshots of 7PSS20-7PA10 systems*

Representative conformations are shown of trajectories at various NaCl concentrations. PA10 molecules are highlighted in red. The Na+ and Cl- ions are highlighted as green and pink spheres, respectively. Results for the three different initial configurations (I, II, and III) are presented in columns.

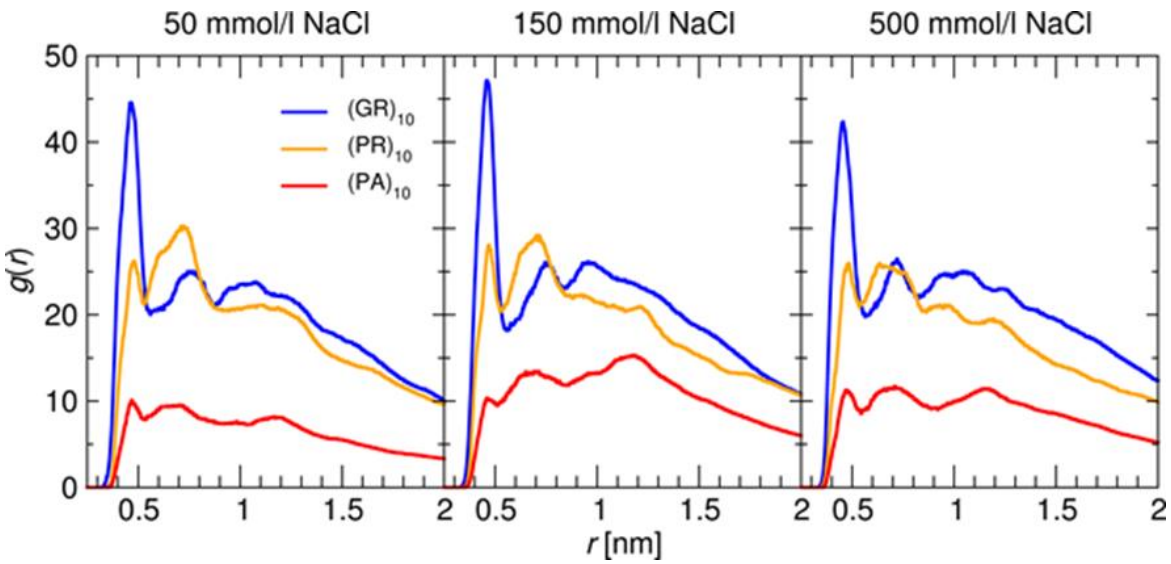

Suppl. Figure S18. The radial distribution function (RDF) between the Cα atoms and S atom

MD simulations of 7 PSS_20 : 7 Peptide systems were run at various NaCl concentrations, averaged over three different initial configurations and analyzed for RDF.

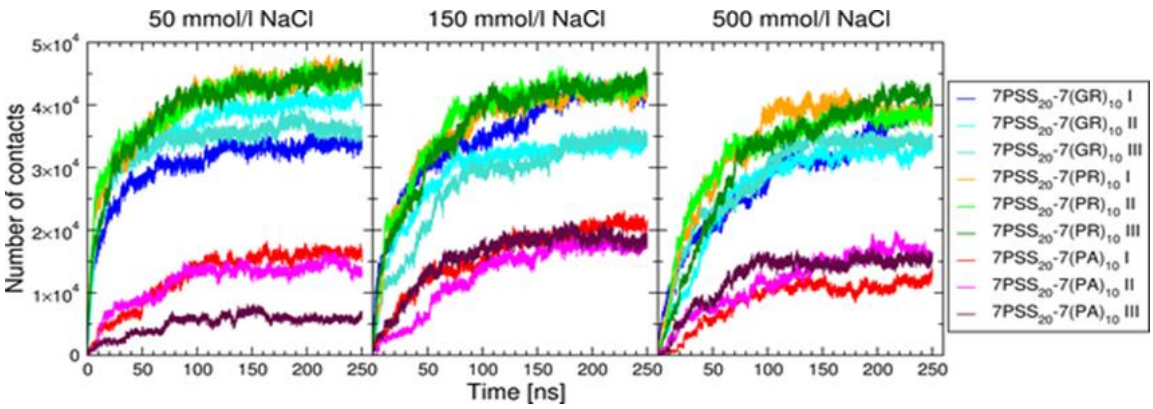

Suppl. Figure S19. *Evolution of the number of contacts*

Evolution of the number of contacts between PSS_20 and R-DPR molecules in 7:7 systems simulated, as a function of the simulation time for systems at various NaCl concentrations.

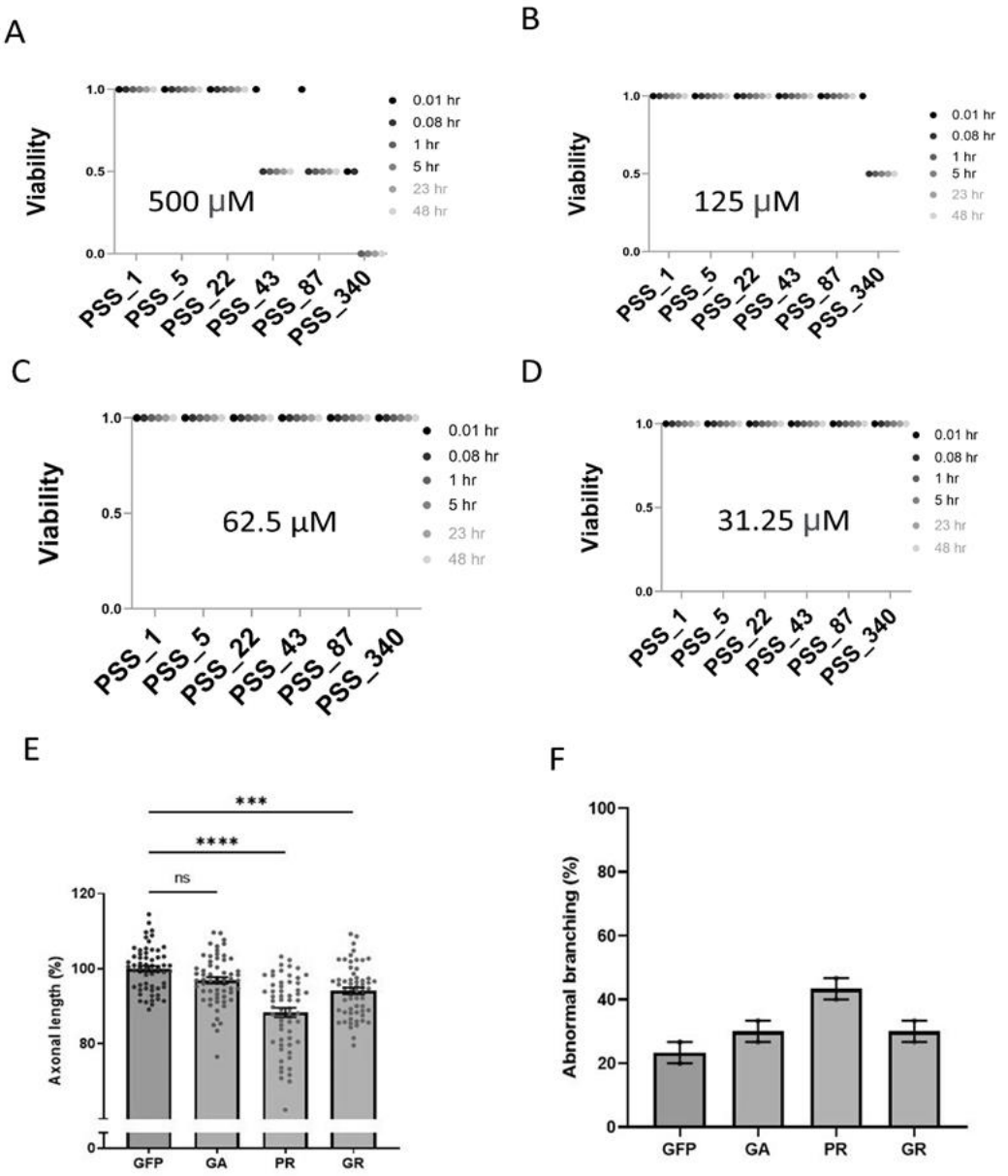

Suppl. Figure S20. *Toxicity of PSS and DPRs in zebra fish embryo*

Zebrafish embryos with chorion were incubated at 500 µM (A), 125 µM (B), 62.5 (C), or 31.25 (D) of different variant of PSS (PSS_1, PSS_5, PSS_ 22, PSS_43, PSS_ 87, PSS_ 340) and were visualised for up to 48 hr. RNA encoding for PR, GR, GA, and GFP was injected at 1-2 cell stages and embryos were dechorionated at 6hpf. Embryo were fixed 30hpf and immunostained with anti SV2 antibody to determine Axonal length (E) and Axonal branching (F).

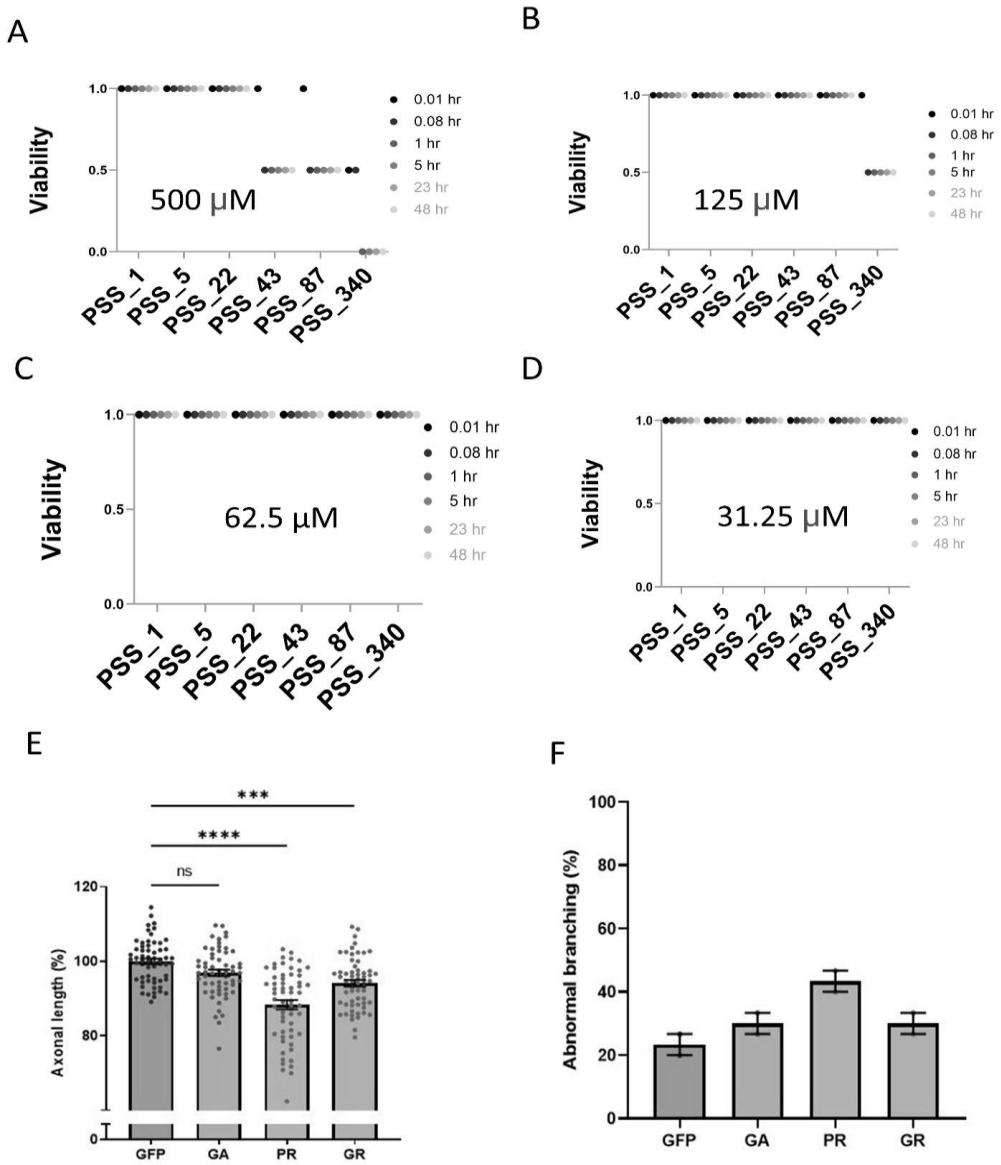

Suppl. Figure S21. Toxicity of PSS and DPRs in zebra fish embryo

Zebrafish embryos with chorion were incubated at 500 µM (A), 125 µM (B), 62.5 (C), or 31.25 (D) of different variant of PSS (PSS_1, PSS_5, PSS_ 22, PSS_43, PSS_ 87, PSS_ 340) and were visualised for up to 48 hr. RNA encoding for PR, GR, GA, and GFP was injected at 1-2 cell stage and embryos were dechorionated at 6hpf. Embryo were fixed 30hpf and immunostained with anti SV2 antibody to determine Axonal length (E) and Axonal branching (F).

Suppl. Table S1

Drugs on the market that contain polystyrene sulfonate (PSS): names, main component and additives.

Name	**Main component**	**Additives**
Kionex ™	Sodium Polystyrene Sulfonate Suspension USP	Sorbitol Solution USP 0.2%, Alcohol per 60 ml, purified water USP, Propylene Glycol USP, Magnesium Aliminum Silicate NF, Xanthan Gum NF, Sodium Saccharin USP, Sorbic Acid NF, Methylparaben NF, Propylparaben NF, and Flavor.
Resonium A	Sodium Polystyrene Sulfonate powder	Saccharin sodium, Vanillin
Sorbisterit	Calcium Polystyrene sulfonate	Saccharin sodium, anhydrous citric acid, mannitol (E421) and lemon flavour (containing: maltodextrin, acacia gum (Gum Arabic, E414) and α- tocopherol (E307))
Tolevamer	Poly(4-styrenesulfonate) with either sodium or a mixture of sodium and potassium as ions	-
Kayexalate	Sodium Polystyrene Sulfonate available as a cream to light brown, finely ground powder	-

Suppl. Table S2. Average number of hydrogen bonds (N_{Hb}) between peptides and the PSS_20 molecule, per single PSS group (MD results for 1:1 PSS-peptide systems at different salt concentrations). Results are averaged over the last 200 ns of simulations.

NaCl concentration **mM**	**System**	**N_{Hb}**
50	1 PSS_20 - 1 GR_{10}	0.67 ± 0.11
	1 PSS_20 - 1 PR_{10}	0.52 ± 0.14
	1 PSS_20 - 1 PA_{10}	0.05 ± 0.05
150	1 PSS_20 - 1 GR_{10}	0.58 ± 0.11
	1 PSS_20 - 1 PR_{10}	0.45 ± 0.12
	1 PSS_20 - 1 PA_{10}	0.04 ± 0.04
500	1 PSS_20 - 1 GR_{10}	0.57 ± 0.10
	1 PSS_20 - 1 PR_{10}	0.41 ± 0.10
	1 PSS_20 - 1 PA_{10}	0.04 ± 0.04

Suppl. Table S3. Average number of hydrogen bonds (N_{Hb}) between peptides and the PSS_20 molecules, per single PSS group (MD results for 7:7 PSS-peptide systems at different salt concentrations). Results are averaged over the last 50 ns of simulations.

NaCl concentration [mmol/l]	**System**	**N_{Hb}**
50	7 PSS_20 - 7 GR_{10}	0.72 ± 0.07
	7 PSS_20 - 7 PR_{10}	0.67 ± 0.07
	7 PSS_20 - 7 PA_{10}	0.04 ± 0.02
150	7 PSS_20 - 7 GR_{10}	0.71 ± 0.07
	7 PSS_20 - 7 PR_{10}	0.65 ± 0.08
	7 PSS_20 - 7 PA_{10}	0.04 ± 0.02
500	7 PSS_20 - 7 GR_{10}	0.74 ± 0.08
	7 PSS_20 - 7 PR_{10}	0.63 ± 0.07
	7 PSS_20 - 7 PA_{10}	0.05 ± 0.02

References

1. Verma, A. (2014) Tale of two diseases: amyotrophic lateral sclerosis and frontotemporal dementia. *Neurol India*. **62**: 347-51.
2. Taylor, J.P., R.H. Brown, Jr., and D.W. Cleveland (2016) Decoding ALS: from genes to mechanism. *Nature*. **539**: 197-206.
3. Mead, R.J., et al. (2023) Amyotrophic lateral sclerosis: a neurodegenerative disorder poised for successful therapeutic translation. *Nat Rev Drug Discov*. **22**: 185-212.
4. Pakravan, D., et al. (2021) Role and therapeutic potential of liquid-liquid phase separation in amyotrophic lateral sclerosis. *J Mol Cell Biol*. **13**: 15-28.
5. DeJesus-Hernandez, M., et al. (2011) Expanded GGGGCC hexanucleotide repeat in noncoding region of C9ORF72 causes chromosome 9p-linked FTD and ALS. *Neuron*. **72**: 245-56.
6. Farg, M.A., et al. (2014) C9ORF72, implicated in amytrophic lateral sclerosis and frontotemporal dementia, regulates endosomal trafficking. *Hum Mol Genet*. **23**: 3579-95.
7. Lee, Y.B., et al. (2013) Hexanucleotide repeats in ALS/FTD form length-dependent RNA foci, sequester RNA binding proteins, and are neurotoxic. *Cell Rep*. **5**: 1178-86.
8. Zu, T., et al. (2013) RAN proteins and RNA foci from antisense transcripts in C9ORF72 ALS and frontotemporal dementia. *Proc Natl Acad Sci U S A*. **110**: E4968-77.
9. Jiang, J. and J. Ravits (2019) Pathogenic Mechanisms and Therapy Development for C9orf72 Amyotrophic Lateral Sclerosis/Frontotemporal Dementia. *Neurotherapeutics*. **16**: 1115-1132.
10. Mackenzie, I.R., et al. (2013) Dipeptide repeat protein pathology in C9ORF72 mutation cases: clinico-pathological correlations. *Acta Neuropathol*. **126**: 859-79.
11. Mori, K., et al. (2013) Bidirectional transcripts of the expanded C9orf72 hexanucleotide repeat are translated into aggregating dipeptide repeat proteins. *Acta Neuropathol*. **126**: 881-93.
12. Chew, J., et al. (2015) Neurodegeneration. C9ORF72 repeat expansions in mice cause TDP-43 pathology, neuronal loss, and behavioral deficits. *Science*. **348**: 1151-4.
13. Stopford, M.J., et al. (2017) C9ORF72 hexanucleotide repeat exerts toxicity in a stable, inducible motor neuronal cell model, which is rescued by partial depletion of Pten. *Hum Mol Genet*. **26**: 1133-1145.
14. Swinnen, B., W. Robberecht, and L. Van Den Bosch (2020) RNA toxicity in non-coding repeat expansion disorders. *EMBO J*. **39**: e101112.
15. Zhang, Y.J., et al. (2019) Heterochromatin anomalies and double-stranded RNA accumulation underlie C9orf72 poly(PR) toxicity. *Science*. **363**
16. Kanekura, K., et al. (2018) Characterization of membrane penetration and cytotoxicity of C9orf72-encoding arginine-rich dipeptides. *Sci Rep*. **8**: 12740.
17. White, M.R., et al. (2019) C9orf72 Poly(PR) Dipeptide Repeats Disturb Biomolecular Phase Separation and Disrupt Nucleolar Function. *Mol Cell*. **74**: 713-728 e6.
18. Van Nerom, M., et al. (2023) C9orf72-linked arginine-rich dipeptide repeats aggravate pathological phase separation of G3BP1. *bioRxiv*.
19. Krishnan, G., et al. (2022) Poly(GR) and poly(GA) in cerebrospinal fluid as potential biomarkers for C9ORF72-ALS/FTD. *Nat Commun*. **13**: 2799.
20. Ash, P.E., et al. (2013) Unconventional translation of C9ORF72 GGGGCC expansion generates insoluble polypeptides specific to c9FTD/ALS. *Neuron*. **77**: 639-46.
21. Gendron, T.F., et al. (2015) Cerebellar c9RAN proteins associate with clinical and neuropathological characteristics of C9ORF72 repeat expansion carriers. *Acta Neuropathol*. **130**: 559-73.
22. Zhu, Q., et al. (2020) Reduced C9ORF72 function exacerbates gain of toxicity from ALS/FTD-causing repeat expansion in C9orf72. *Nat Neurosci*. **23**: 615-624.

23. Miyaji, Y., et al. (2015) Effect of edaravone on favorable outcome in patients with acute cerebral large vessel occlusion: subanalysis of RESCUE-Japan Registry. *Neurol Med Chir (Tokyo)*. **55**: 241-7.
24. Petrov, D., et al. (2017) ALS Clinical Trials Review: 20 Years of Failure. Are We Any Closer to Registering a New Treatment? *Front Aging Neurosci*. **9**: 68.
25. Miller, R.G., et al. (2002) Riluzole for amyotrophic lateral sclerosis (ALS)/motor neuron disease (MND). *Cochrane Database Syst Rev*. CD001447.
26. Smith, R., et al. (2017) Enhanced Bulbar Function in Amyotrophic Lateral Sclerosis: The Nuedexta Treatment Trial. *Neurotherapeutics*. **14**: 762-772.
27. Miller, T.M., et al. (2022) Trial of Antisense Oligonucleotide Tofersen for SOD1 ALS. *N Engl J Med*. **387**: 1099-1110.
28. Lagier-Tourenne, C., et al. (2013) Targeted degradation of sense and antisense C9orf72 RNA foci as therapy for ALS and frontotemporal degeneration. *Proc Natl Acad Sci U S A*. **110**: E4530-9.
29. Tran, H., et al. (2022) Suppression of mutant C9orf72 expression by a potent mixed backbone antisense oligonucleotide. *Nat Med*. **28**: 117-124.
30. Consortium, *Study of WVE-004 in Patients With C9orf72-associated Amyotrophic Lateral Sclerosis (ALS) or Frontotemporal Dementia (FTD): NCT04931862*. 2021: https://clinicaltrials.gov/ct2/show/NCT04931862.
31. Allolio, C., et al. (2018) Arginine-rich cell-penetrating peptides induce membrane multilamellarity and subsequently enter via formation of a fusion pore. *Proc Natl Acad Sci U S A*. **115**: 11923-11928.
32. Shi, K.Y., et al. (2017) Toxic PR(n) poly-dipeptides encoded by the C9orf72 repeat expansion block nuclear import and export. *Proc Natl Acad Sci U S A*. **114**: E1111-E1117.
33. Lin, Y., et al. (2016) Toxic PR Poly-Dipeptides Encoded by the C9orf72 Repeat Expansion Target LC Domain Polymers. *Cell*. **167**: 789-802 e12.
34. Borgia, A., et al. (2018) Extreme disorder in an ultrahigh-affinity protein complex. *Nature*. **555**: 61-66.
35. Hunt, T.V., et al. (2019) Single-dose sodium polystyrene sulfonate for hyperkalemia in chronic kidney disease or end-stage renal disease. *Clin Kidney J*. **12**: 408-413.
36. Wang, X., et al. (2023) Efficacy and safety of calcium polystyrene sulfonate in patients with hyperkalemia and stage 3-5 non-dialysis chronic kidney disease: a single-center randomized controlled trial. *J Int Med Res*. **51**: 3000605231167516.
37. Bratek-Skicki, A., J. Ahmed, and P. Tompa, *Means and methods to treat neurodegenerative diseases*. 2023.
38. de Assunção, R.M.N., et al. (2005) Synthesis, characterization, and application of the sodium poly(styrenesulfonate) produced from waste polystyrene cups as an admixture in concrete. *J. Appl. Polymer Sci.* **96**: 1534-1538.
39. Chen, S.-L., et al. (2004) Ion exchange resin/polystyrene sulfonate composite membranes for PEM fuel cells. *J. Membrane Sci.* **243**: 327-333.
40. Ahmad, M., et al. (2020) Heterogeneous ion exchange membranes based on thermoplastic polyurethane (TPU): effect of PSS/DVB resin on morphology and electrodialysis. *RSC Adv*. **10**: 3029-3039.
41. Kawan, A., *Wrinkle masking composition of sodium polystyrene sulfonate and process for use*. 1989.
42. Parks, M. and D. Grady (2019) Sodium Polystyrene Sulfonate for Hyperkalemia. *JAMA Intern Med*. **179**: 1023-1024.
43. Dunn, J.D., et al. (2015) The burden of hyperkalemia in patients with cardiovascular and renal disease. *Am J Manag Care*. **21**: s307-15.
44. Vander Straeten, A., et al. (2017) Protein-polyelectrolyte complexes to improve the biological activity of proteins in layer-by-layer assemblies. *Nanoscale*. **9**: 17186-17192.
45. Vander Straeten, A., et al. (2018) Integrating Proteins in Layer-by-Layer Assemblies Independently of their Electrical Charge. *ACS Nano*. **12**: 8372-8381.

46. Freibaum, B.D. and J.P. Taylor (2017) The Role of Dipeptide Repeats in C9ORF72-Related ALS-FTD. *Front Mol Neurosci*. **10**: 35.
47. Broecker, J., C. Vargas, and S. Keller (2011) Revisiting the optimal c value for isothermal titration calorimetry. *Anal Biochem*. **418**: 307-9.
48. Aguzzi, A. and M. Altmeyer (2016) Phase Separation: Linking Cellular Compartmentalization to Disease. *Trends Cell Biol*. **26**: 547-558.
49. Altmeyer, M., et al. (2015) Liquid demixing of intrinsically disordered proteins is seeded by poly(ADP-ribose). *Nat Commun*. **6**: 8088.
50. Patel, A., et al. (2015) A Liquid-to-Solid Phase Transition of the ALS Protein FUS Accelerated by Disease Mutation. *Cell*. **162**: 1066-77.
51. Boeynaems, S., et al. (2017) Phase Separation of C9orf72 Dipeptide Repeats Perturbs Stress Granule Dynamics. *Mol Cell*. **65**: 1044-1055 e5.
52. Boeynaems, S., et al. (2019) Spontaneous driving forces give rise to protein-RNA condensates with coexisting phases and complex material properties. *Proc Natl Acad Sci U S A*. **116**: 7889-7898.
53. O'Donoghue, P., J. Ling, and D. Soll (2018) Transfer RNA function and evolution. *RNA Biol*. **15**: 423-426.
54. Biancalana, M. and S. Koide (2010) Molecular mechanism of Thioflavin-T binding to amyloid fibrils. *Biochim Biophys Acta*. **1804**: 1405-12.
55. Tayeb-Fligelman, E., et al. (2021) Inhibition of amyloid formation of the Nucleoprotein of SARS-CoV-2. *bioRxiv*.
56. Balendra, R. and A.M. Isaacs (2018) C9orf72-mediated ALS and FTD: multiple pathways to disease. *Nat Rev Neurol*. **14**: 544-558.
57. Banerjee, P.R., et al. (2017) Reentrant Phase Transition Drives Dynamic Substructure Formation in Ribonucleoprotein Droplets. *Angew Chem Int Ed Engl*. **56**: 11354-11359.
58. Milin, A.N. and A.A. Deniz (2018) Reentrant Phase Transitions and Non-Equilibrium Dynamics in Membraneless Organelles. *Biochemistry*. **57**: 2470-2477.
59. Guillen-Boixet, J., et al. (2020) RNA-Induced Conformational Switching and Clustering of G3BP Drive Stress Granule Assembly by Condensation. *Cell*. **181**: 346-361 e17.
60. Coughlin, J.E., et al. (2013) Sulfonation of polystyrene: Toward the “ideal” polyelectrolyte. *Polymer Chem.* **51**: 2416-2424.
61. Fu, J. and J.B. Schlenoff (2016) Driving Forces for Oppositely Charged Polyion Association in Aqueous Solutions: Enthalpic, Entropic, but Not Electrostatic. *J Am Chem Soc*. **138**: 980-90.
62. Kramer, N.J., et al. (2018) CRISPR-Cas9 screens in human cells and primary neurons identify modifiers of C9ORF72 dipeptide-repeat-protein toxicity. *Nat Genet*. **50**: 603-612.
63. Kwon, I., et al. (2014) Poly-dipeptides encoded by the C9orf72 repeats bind nucleoli, impede RNA biogenesis, and kill cells. *Science*. **345**: 1139-45.
64. Lee, K.H., et al. (2016) C9orf72 Dipeptide Repeats Impair the Assembly, Dynamics, and Function of Membrane-Less Organelles. *Cell*. **167**: 774-788 e17.
65. Swinnen, B., et al. (2018) A zebrafish model for C9orf72 ALS reveals RNA toxicity as a pathogenic mechanism. *Acta Neuropathol*. **135**: 427-443.
66. Bartoletti, M., et al. (2019) Phenotypic Suppression of ALS/FTD-Associated Neurodegeneration Highlights Mechanisms of Dysfunction. *J Neurosci*. **39**: 8217-8224.
67. Tang, X., et al. (2020) Divergence, Convergence, and Therapeutic Implications: A Cell Biology Perspective of C9ORF72-ALS/FTD. *Mol Neurodegener*. **15**: 34.
68. Frottin, F., et al. (2021) Multiple pathways of toxicity induced by C9orf72 dipeptide repeat aggregates and G(4)C(2) RNA in a cellular model. *Elife*. **10**
69. Radwan, M., et al. (2020) Arginine in C9ORF72 Dipolypeptides Mediates Promiscuous Proteome Binding and Multiple Modes of Toxicity. *Mol Cell Proteomics*. **19**: 640-654.

70. Corman, A., et al. (2019) A Chemical Screen Identifies Compounds Limiting the Toxicity of C9ORF72 Dipeptide Repeats. *Cell Chem Biol*. **26**: 235-243 e5.
71. Tran, H., et al. (2015) Differential Toxicity of Nuclear RNA Foci versus Dipeptide Repeat Proteins in a Drosophila Model of C9ORF72 FTD/ALS. *Neuron*. **87**: 1207-1214.
72. Mizielinska, S., et al. (2014) C9orf72 repeat expansions cause neurodegeneration in Drosophila through arginine-rich proteins. *Science*. **345**: 1192-1194.
73. Sterns, R.H., et al. (2010) Ion-exchange resins for the treatment of hyperkalemia: are they safe and effective? *J Am Soc Nephrol*. **21**: 733-5.
74. Lopez, S. and F. He (2022) Spinocerebellar Ataxia 36: From Mutations Toward Therapies. *Front Genet*. **13**: 837690.
75. Reyes, C.J., et al. (2021) Brain Regional Differences in Hexanucleotide Repeat Length in X-Linked Dystonia-Parkinsonism Using Nanopore Sequencing. *Neurol Genet*. **7**: e608.
76. Zu, T., et al. (2017) RAN Translation Regulated by Muscleblind Proteins in Myotonic Dystrophy Type 2. *Neuron*. **95**: 1292-1305 e5.
77. Boeynaems, S. and e. al. (2023) Aberrant phase separation is a common killing strategy of positively charged peptides in biology and human disease. *bioRxiv*. **doi: https://doi.org/10.1101/2023.03.09.531820**
78. Berendsen, H.J.C., D. van der Spoel, and R. van Drunen (1995) GROMACS: A message-passing parallel molecular dynamics implementation. *Computer Phys. Commun.* **91**: 43-56.
79. Abraham, M.J., et al. (2015) GROMACS: High performance molecular simulations through multi-level parallelism from laptops to supercomputers. *SoftwareX*. **1-2**: 19-25.
80. Pronk, S., et al. (2013) GROMACS 4.5: a high-throughput and highly parallel open source molecular simulation toolkit. *Bioinformatics*. **29**: 845-54.
81. Jorgensen, W.L. and J. Tirado-Rives (1988) The OPLS [optimized potentials for liquid simulations] potential functions for proteins, energy minimizations for crystals of cyclic peptides and crambin. *J Am Chem Soc*. **110**: 1657-66.
82. Batys, P., et al. (2020) pH-Induced Changes in Polypeptide Conformation: Force-Field Comparison with Experimental Validation. *J Phys Chem B*. **124**: 2961-2972.
83. Pandey, P.R. and S. Roy (2012) Distinctions in early stage unwinding mechanisms of zwitterionic, capped, and neutral forms of different alpha-helical homopolymeric peptides. *J Phys Chem B*. **116**: 4731-40.
84. Batys, P., et al. (2019) Comparing water-mediated hydrogen-bonding in different polyelectrolyte complexes. *Soft Matter*. **15**: 7823-7831.
85. Batys, P., et al. (2018) Hydration and Temperature Response of Water Mobility in Poly(diallyldimethylammonium)-Poly(sodium 4-styrenesulfonate) Complexes. *Macromolecules*. **51**: 8268-8277.
86. Åqvist, J. (1990) Ion-water interaction potentials derived from free energy perturbation simulations. *J. Phys. Chem*. **94**: 8021–8024.
87. Chandrasekhar, J., D.C. Spellmeyer, and W.L. Jorgensen (1984) Energy component analysis for dilute aqueous solutions of lithium(1+), sodium(1+), fluoride(1-), and chloride(1-) ions. *J. Am. Chem. Soc.* **106**: 903–910.
88. Jorgensen, W.L. and J.D. Madura (1985) Temperature and size dependence for Monte Carlo simulations of TIP4P water. *Mol. Phys.* **56**: 1381-1392.
89. Bussi, G., D. Donadio, and M. Parrinello (2007) Canonical sampling through velocity rescaling. *J Chem Phys*. **126**: 014101.
90. Rahman, A. (1981) Polymorphic transitions in single crystals: A new molecular dynamics method. *J. Appl. Phys.* **52**: 7182.
91. Essmann, U., L. Perera, and M.L. Berkowitz (1995) A smooth particle mesh Ewald method. *J. Chem. Phys.* **103**: 8577.
92. Hess, B. (2008) P-LINCS: A Parallel Linear Constraint Solver for Molecular Simulation. *J Chem Theory Comput*. **4**: 116-22.

93. Miyamoto, S. and P.A. Kollman (1992) Settle: An analytical version of the SHAKE and RATTLE algorithm for rigid water models. *J. Comput. Chem.* **13**: 919-1035.
94. Humphrey, W., A. Dalke, and K. Schulten (1996) VMD: visual molecular dynamics. *J Mol Graph*. **14**: 33-8, 27-8.